

TIC

LOW-TEMPERATURE ELECTRON IRRADIATION AND
ANNEALING IN PURE MAGNESIUM

NOTICE

**PORTIONS OF THIS REPORT ARE ILLEGIBLE. It
has been reproduced from the best available
copy to permit the broadest possible avail-
ability.**

BY

JAMES HARRY SIMESTER

B.A., Ohio Wesleyan University, 1974

M.S., University of Illinois, 1976

THESIS

Submitted in partial fulfillment of the requirements
for the degree of Doctor of Philosophy in Physics
in the Graduate College of the
University of Illinois at Urbana-Champaign, 1982

MASTER

Urbana, Illinois

PACS numbers: 61.80.Fe

61.70.Bv

DISTRIBUTION OF THIS DOCUMENT IS UNLIMITED

DISCLAIMER

This report was prepared as an account of work sponsored by an agency of the United States Government. Neither the United States Government nor any agency Thereof, nor any of their employees, makes any warranty, express or implied, or assumes any legal liability or responsibility for the accuracy, completeness, or usefulness of any information, apparatus, product, or process disclosed, or represents that its use would not infringe privately owned rights. Reference herein to any specific commercial product, process, or service by trade name, trademark, manufacturer, or otherwise does not necessarily constitute or imply its endorsement, recommendation, or favoring by the United States Government or any agency thereof. The views and opinions of authors expressed herein do not necessarily state or reflect those of the United States Government or any agency thereof.

DISCLAIMER

Portions of this document may be illegible in electronic image products. Images are produced from the best available original document.

DOE/ER/01198--1373

DE82 011775

LOW-TEMPERATURE ELECTRON IRRADIATION AND
ANNEALING IN PURE MAGNESIUM

BY

JAMES HARRY SIMESTER

B.A., Ohio Wesleyan University, 1974
M.S., University of Illinois, 1976

THESIS

Submitted in partial fulfillment of the requirements
for the degree of Doctor of Philosophy in Physics
in the Graduate College of the
University of Illinois at Urbana-Champaign, 1982

DISCLAIMER

This book was prepared as an account of work sponsored by an agency of the United States Government. Neither the United States Government nor any agency thereof, nor any of their employees, makes any warranty, express or implied, or assumes any legal liability or responsibility for the accuracy, completeness, or usefulness of any information, apparatus, product, or process disclosed, or represents that its use would not infringe privately owned rights. Reference herein to any specific commercial product, process, or service by trade name, trademark, manufacturer, or otherwise, does not necessarily constitute or imply its endorsement, recommendation, or favoring by the United States Government or any agency thereof. The views and opinions of authors expressed herein do not necessarily state or reflect those of the United States Government or any agency thereof.

Urbana, Illinois

PACS numbers: 61.80.Fe

61.70.Bv

DISTRIBUTION OF THIS DOCUMENT IS UNLIMITED

MGW

LOW TEMPERATURE ELECTRON IRRADIATION AND
ANNEALING IN PURE MAGNESIUM

James Harry Simester, Ph.D.
Department of Physics
University of Illinois at Urbana-Champaign, 1982

In this study of magnesium after 1.0 MeV electron irradiations at 1.55 K, it has been observed that the damage production rate in Mg is $(3.57 \pm 0.03) \times 10^{-26} \Omega\text{cm}/(e^- \text{cm}^2)$. There is no evidence for thermal annealing up to 4 K. The low temperature recovery in magnesium is found to consist of two broad substages between 4-14 K, both of which exhibit evidence for correlated and uncorrelated recovery processes. The two substages are found to have very different frequency factors for annealing, and there is evidence that the recovery processes in the second substage are influenced by those in the first. Theoretical calculations are found to favor an octahedral configuration or a split dumbbell configuration along one of the close-packed rows in the basal plane for the interstitial as opposed to the split dumbbell along the c axis which has been found for zinc. A model for recovery is proposed using the split configuration in the plane which explains the first substage as being due to interstitial migration in the basal plane and the second to migration perpendicular to the plane.

ACKNOWLEDGMENTS

I would like to thank my advisor, Professor James S. Koehler, for suggesting this project and for his continued guidance and support throughout the course of the investigation.

I am grateful for the helpful suggestions and encouragement of many of my fellow graduate students and colleagues, particularly Bob Kozlowski, Yan Lwin, Maria Menendez, and Jim Watson. I also owe much to the technical staff of the Materials Research Laboratory and the Physics Department, particularly to Brad Clymer for his proficient handling of the accelerator.

I am indebted to Dr. Tom Dillman, whose teaching, counsel, and boundless enthusiasm helped stimulate and develop my interest in physics, and whose friendship has meant much to me.

I thank my parents, Harry and Helen, for their unflagging support, optimism, and confidence in me throughout my academic career.

Finally, I offer a note of personal thanks to my fiancée, Karen Huber, for her patience and understanding in the face of the many long hours and late nights I have spent in the lab to produce the results presented herein.

This research was supported by the Department of Energy under contract DE-AC02-76ER01198.

TABLE OF CONTENTS

CHAPTER	Page
I. INTRODUCTION.....	1
II. EXPERIMENTAL APPARATUS AND PROCEDURE.....	4
A. Sample Preparation.....	4
B. Cryostat.....	7
C. Electron Beam.....	16
D. Thermometry and Temperature Measurement.....	20
E. Resistivity Measurements.....	25
F. Anneals.....	26
III. EXPERIMENTAL RESULTS AND ANALYSIS.....	28
A. Damage Production.....	28
B. Isochronal Anneals.....	28
C. Isothermal Anneals.....	35
D. Activation Energy Analysis.....	38
1. Slope Change Analysis.....	38
2. Primak Analysis.....	38
3. Discussion.....	43
E. Radiation Doping.....	52
F. Other Results.....	61
G. Summary and Comparison to Other Experiments.....	64
IV. THEORETICAL MODEL FOR RECOVERY.....	71
A. Interstitial Model Calculations.....	71
1. Procedure.....	71
2. Potential.....	72
3. Configurations.....	73
B. Recovery Model.....	77
V. CONCLUSIONS.....	83
APPENDIX A ANALYSIS OF MAGNESIUM USED FOR SAMPLE GROWTH.....	84
APPENDIX B DETAILS OF SAMPLE GROWTH AND THINNING PROCEDURES.....	85
APPENDIX C SIMPLE THEORY FOR RECOVERY KINETICS.....	87
APPENDIX D SLOPE CHANGE ACTIVATION ENERGY ANALYSIS.....	89
APPENDIX E PRIMAK ACTIVATION ENERGY ANALYSIS.....	92

Page

REFERENCES.....	96
VITA.....	99

I. INTRODUCTION

When a metal is irradiated with electrons at low temperature, the resulting introduction of defects (vacancies and interstitials) will cause an increase in its resistivity. This increase is proportional to the defect concentration for sufficiently low concentrations. As the sample temperature is subsequently raised, there is a recovery of the resistivity as the defects acquire thermal energy which allows them to become mobile and anneal. In general, this annealing process does not occur continuously with temperature, but rather at fairly discrete temperatures in distinct stages, the lowest of which is called stage I.

In the face centered cubic (f.c.c.) metals, the most extensively studied crystallographic group, stage I is comprised of five distinct substages, A through E. The temperatures of the four lowest substages are independent of defect concentration. Substages A, B, and C correspond to the recombination of vacancy-interstitial close pairs. Substage D is thought to represent either a spectrum of nearly identical widely spaced close pairs^{1/} or correlated long-range recovery of interstitials with their own vacancies.^{2/} Substage E moves to lower temperatures with increasing initial defect concentrations and is associated with free long-range migration of the interstitial.

The f.c.c. interstitial is found to have a stable configuration wherein the interstitial and a lattice atom share the latter's lattice position in the form of a dumbbell centered on the normal lattice site.^{3/} The dumbbell is oriented along the (100) direction.

Among the f.c.c. metals investigated, only gold is anomalous, showing more or less continuous recovery beginning below 2 K.^{4/}

By contrast, the low temperature annealing behavior of the hexagonal metals is not at all well understood. Thus far, most of the annealing studies following irradiations of the hexagonals have been made using relatively impure samples, which can obscure or completely alter the details of the recovery substructure. Results for cobalt and gadolinium,^{5/} zinc,^{6/} and zirconium^{7/} showed evidence of similarities to the pattern of f.c.c. recovery, i.e., a series of close-pair substages followed by a dose-dependent substage. Studies of cadmium after thermal neutron irradiation showed a "see-saw" effect whereby the relative recovery below 26 K decreased with increasing irradiation dose.^{8/} This feature has not been observed for any other hexagonal metal. In addition, no clear evidence for a concentration dependent substage has been found in cadmium.

Using diffuse x-ray scattering, Ehrhart and Schönfeld^{9/} have found the interstitial in zinc to be dumbbell oriented along the c axis. It is not known whether this result is the general case for the hexagonals.

O'Neal and Chaplin^{10/} have studied the recovery of resistivity in magnesium after 0.125-0.40 MeV electron irradiations near 5 K. They found two major low temperature substages, both of which seemed independent of dose. The lower substage was ascribed to a superposition of the annealing of several close pairs. Diffuse x-ray scattering experiments performed by Schönfeld and Ehrhart^{11/} following 3 MeV electron irradiations near 5 K showed the formation of small clusters of 2-3 interstitials during irradiation. The cluster size was found to increase during annealing.

Magnesium should be an interesting hexagonal metal to investigate because its c/a ratio is 1.623, very near the ideal close-packed ratio of 1.633. The vacancy in magnesium has a formation energy of 0.79 ± 0.03 eV^{12/} and an activation energy for self-diffusion of 1.40 eV along the c axis and 1.39 eV perpendicular to the c axis.^{13/} The vacancy anneals between -60° C and 10° C.^{12,14/}

II. EXPERIMENTAL APPARATUS AND PROCEDURE

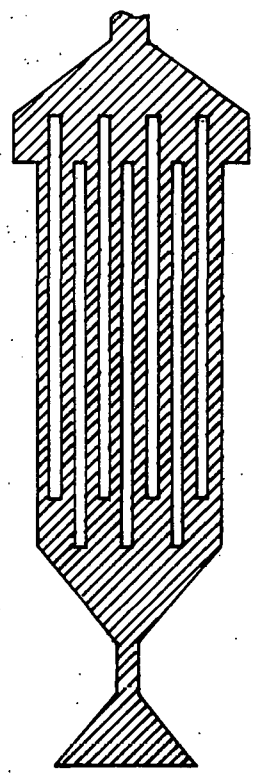
A. Sample Preparation

Single crystals of high purity magnesium were grown from the melt in a split graphite crucible using the Bridgman technique. Starting material was triply distilled polycrystalline magnesium provided by the Dow Chemical Company (see Appendix A for analysis). The grown samples were thinned chemically in a solution of 15% nitric acid and 85% distilled water by volume. The details of the sample growth and thinning procedures are given in Appendix B. The final nominal dimensions of the samples were: length: 19.1 cm; width: 0.027 cm; thickness: 0.011 cm.

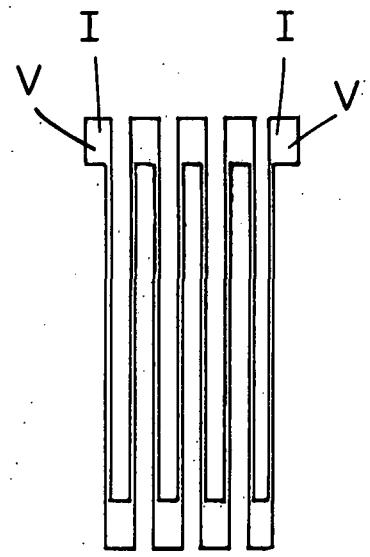
Current and voltage leads of 0.15 mm copper wire were spot-welded to the tabs of each sample (Figure 1). To assure good welds and prevent sparking, it was necessary to perform the spot-welding in a glove bag in a continuously flowing atmosphere of helium gas. The tabs were lightly etched in a dilute citric acid solution, then rinsed in distilled water inside the glove bag to remove any oxide layer before the welds were made. The sample was supported mechanically on a glass slide during the welding process.

Once the leads were attached, each sample was annealed for five hours at 360° C in a vacuum of 2×10^{-6} torr to remove any defects resulting from cold working of the sample during thinning and spot-welding. The sample was then mounted to the OFHC copper sample plate using GE 7031 varnish and the support strips between the legs were cut away. Electrical insulation was provided by a 0.001" sheet of mylar varnished to the sample plate.

Figure 1. Magnesium sample (a) as grown, and (b) after thinning and cutting away support strips, with spot-welded potential and current leads.



(a)



(b)

Sample purity was checked by measuring the ratio of the electrical resistivity between room temperature and 4.2 K. Ratios between 1500-2000 were found (not size-corrected). The geometrical factors used for converting the measured electrical resistance to resistivity were determined experimentally for each sample. They fell in the range $7.0-7.5 \times 10^4 \text{ cm}^{-1}$.

B. Cryostat

The commercial 10 liter liquid helium dewar, vacuum housing, and accelerator hook-up are shown in Figure 2. Figure 3 is a cross-sectional view of the cryostat, indicating the locations of the sample chamber and the superfluid helium refrigerator.

A needle valve was used to allow liquid helium at atmospheric pressure to enter the refrigerator from the dewar helium reservoir. Cooling was then achieved by pumping on the liquid helium in the refrigerator via a 3/4" pump-out tube running from the top of the refrigerator to the top of the cryostat (Figure 4). The pump-out tube was connected by 1.5" tubing to a 24 liter/sec mechanical pump through a 1" valve which could be used to throttle the pump. With the needle valve closed, an ultimate temperature of 1.3 K was attained.

To prevent undue warming of the refrigerator when the needle valve was opened for filling, an impedance tube consisting of a #24 (0.02") chromel A wire threaded tightly through a cupronickel capillary (1/32" O.D. \times 0.003" W.) was installed in series with the needle valve (Figure 5). The impedance tube helped to sustain the pressure difference between the dewar and the refrigerator by restricting the flow of the 4.2 K liquid helium. As a result, the refrigerator could maintain a temperature of 1.65 K with the needle valve open.

Figure 2. Exterior cryostat and accelerator hook-up assembly.

- (A) Commercial 10 liter helium dewar
- (B) Vacuum housing with vacuum common to dewar
- (C) Gate valve
- (D) Flange to accelerator
- (E) Beam direction
- (F) Flange containing 0.002" aluminum scattering foil
- (G) Drift tube
- (H) Radiation shield
- (I) Faraday cup, insulated from the vacuum housing
- (J) Atmospheric vent manifold for helium dewar
- (K) Refrigerator manifold, thermally insulated from the vent manifold by the stainless steel pump-out tube (O)
- (L) To helium pump
- (M) Vacuum feed-through for electrical wires
- (N) Wires for current and voltage measurements, thermometers, and sample heater
- (P) Needle valve

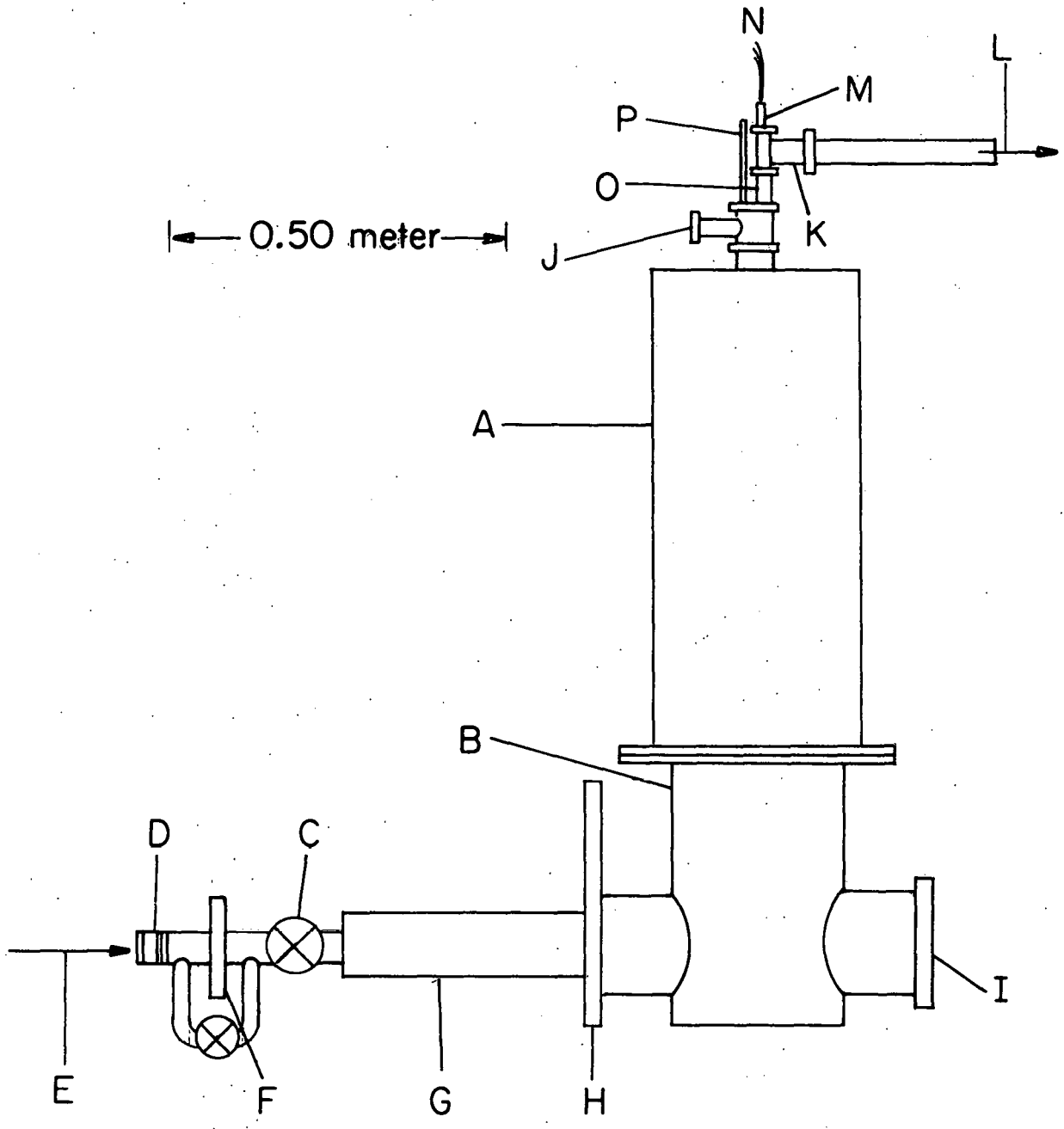


Figure 3. Cross section of cryostat assembly.

- (A) Commercial helium dewar
- (B) Vacuum housing
- (H) Radiation shield
- (I) Faraday cup
- (O) Pump-out tube
- (P) Needle valve
- (R) Refrigerator assembly
- (S) Sample chamber
- (T) Liquid nitrogen
- (U) Liquid helium
- (V) 78 K radiation shield
- (W) 4.2 K radiation shield

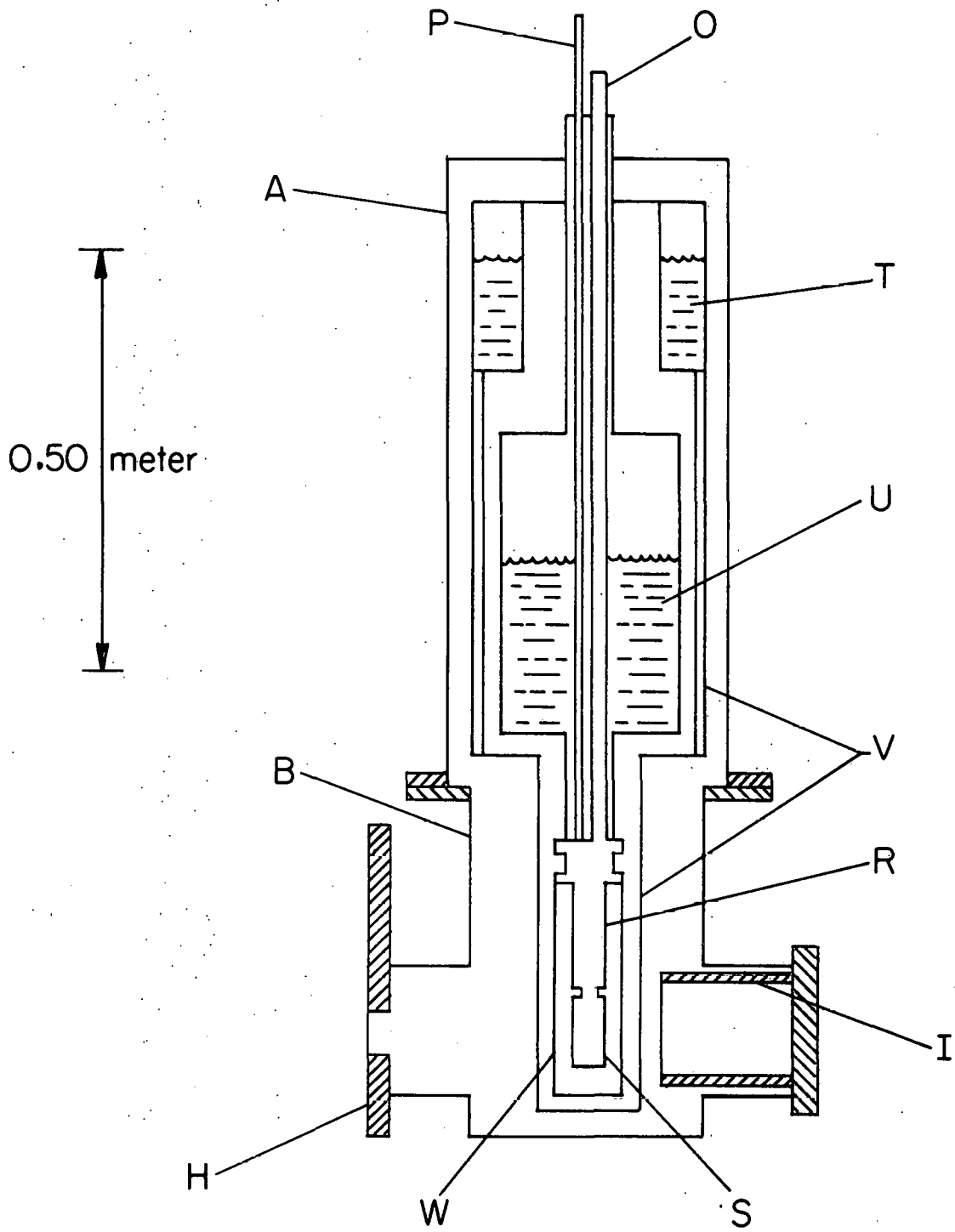


Figure 4. Cross section schematic of refrigerator.

- (A) Pump-out tube
- (B) Needle valve drawn with threading and male piece
omitted for clarity
- (C) Indium o-ring flange
- (D) Needle valve seat
- (E) Impedance tube
- (F) Copper thermal binding post
- (G) Liquid reservoir
- (H) Sample chamber
- (I) Sample plate

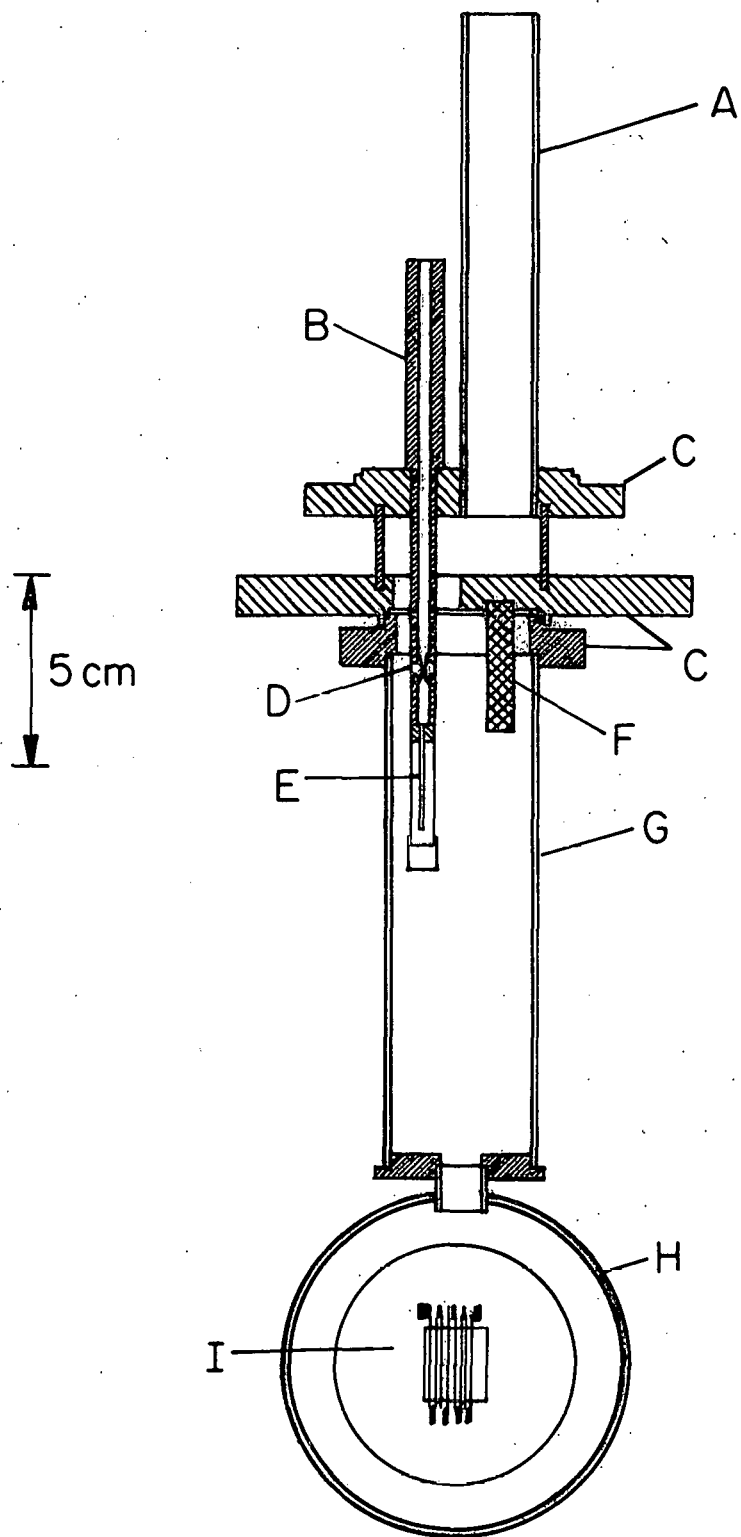
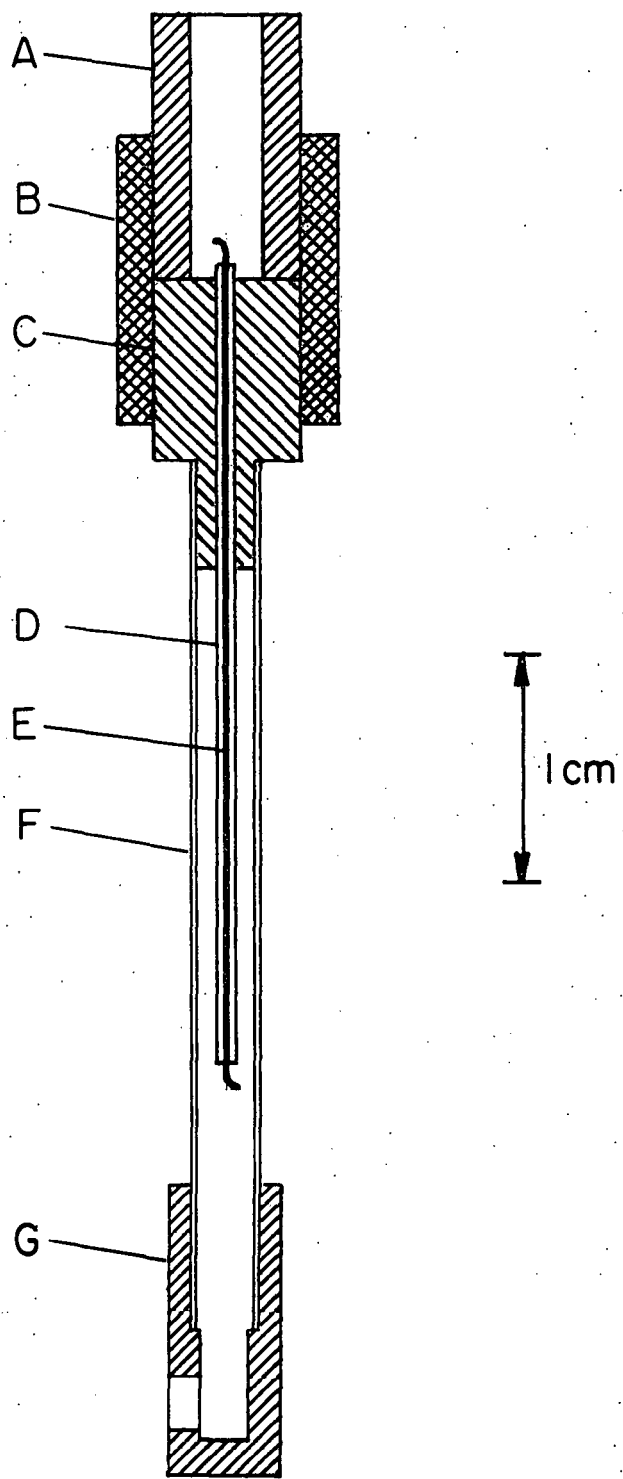


Figure 5. Cross section diagram of impedance tube.

- (A) Base of needle valve
- (B) 1/4" copper fitting
- (C) Copper plug
- (D) Cupronickel capillary tube
- (E) #24 chromel A wire
- (F) Stainless steel tube
- (G) Copper nozzle



The sample chamber, located directly below the refrigerator reservoir, consisted of front and back plates sealed to the main chamber with indium o-rings. 0.001" stainless steel windows soldered to each plate permitted the electron beam to enter and exit from the chamber, passing through the sample and 3/16" of superfluid helium. The sample plate was mounted to the front plate of the chamber, offset by four nylon screws to provide thermal insulation for annealing.

During irradiations the refrigerator was operated with the needle valve closed to achieve maximum cooling power. Two 200 Ω 1/8 watt Allen-Bradley resistors located in the refrigerator reservoir (one near the top, the other just above the sample chamber) were used as a superfluid helium level detector. When the liquid level became low, the electron beam was electrostatically steered away from the cryostat and the needle valve opened remotely. Once the reservoir was full, the needle valve was closed and the beam steered back into the cryostat.

All electrical leads from the refrigerator were connected to a copper thermal binding post at 4.2 K with GE 7031 varnish, then passed out of the cryostat through the pump-out tube. All sample potential leads were passed continuously to the measuring system.

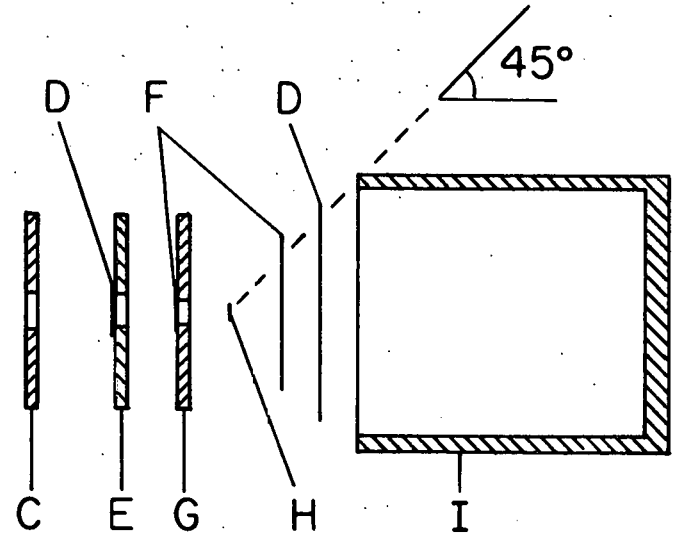
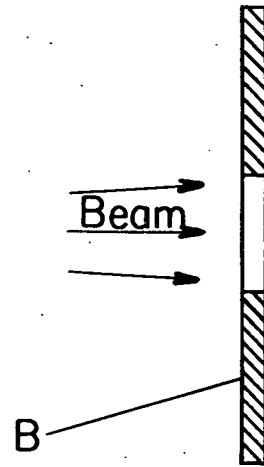
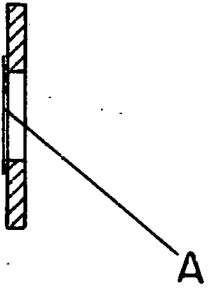
C. Electron Beam

Electrons at 1.10 ± 0.01 MeV were provided by a High Voltage Engineering Van de Graaff accelerator. The electron beam was magnetically deflected 90° to provide even greater stability. A schematic of the beam collimation system appears in Figure 6.

Collimators at room temperature and attached to the nitrogen and helium radiation shields reduced the area of the beam to match the window

Figure 6. Electron beam collimation system shown in horizontal cross section. All collimators are 0.25" thick.

- (A) 0.002" aluminum scattering foil
- (B) Radiation shield
- (C) Room temperature collimator
- (D) 0.001" aluminized mylar window
- (E) Liquid nitrogen temperature collimator
- (F) 0.001" aluminized mylar window
- (G) Liquid helium temperature collimator
- (H) Sample with sample chamber omitted
- (I) Faraday cup



20 cm

of the sample chamber. The two low temperature collimators were covered with foils of 0.001" aluminized mylar. The cryostat, sample chamber, and all of the collimators were aligned with the accelerator beam tube using cross hairs both optically and with a laser.

The 0.002" aluminum foil which separates the accelerator and cryostat vacuums was used to scatter the electrons to provide better spatial homogeneity of the beam. For the foil, electron multiple scattering theory predicts a Gaussian distribution for the scattered beam;^{15/} for 1.1 MeV electrons, the mean scattering angle at which the distribution falls to 1/e of its maximum value is 11.35°. Since the sample chamber spans an angle of 0.86° from the center of the scattering foil, the beam uniformity was expected to vary by about 0.6% over the sample region. In actual practice, fluctuations in the beam energy and in the current to the 90° bending magnet resulted in variations of about 5%.

After passing through the sample chamber, all electrons making angles of less than 45° with the center of the chamber were collected in the Faraday cup and integrated on an Elcor model A309B Current Integrator. The mean scattering angle for the magnesium sample is 16°, for which 99.96% of the beam will be scattered within 45°. Since the sample only blocks 16% of the beam area, it accounts for almost no losses to the Faraday cup. For the liquid helium bath the mean scattering angle is a negligibly small 14°. The angle for the 0.001" stainless steel sample chamber windows is about 20°. Considering both windows, about 2% of the electrons entering the sample chamber will not be collected in the Faraday cup.

The energy loss in all of the foils and in the helium bath prior to reaching the sample was $0.1 \text{ MeV} \cdot \frac{16}{1}$. Thus, the net energy of the electron beam incident on the magnesium sample was $1.00 \pm 0.01 \text{ MeV}$ for all irradiations.

D. Thermometry and Temperature Measurement

Figure 7 is a diagram of the sample plate with the sample attached showing the locations of the three 200Ω 1/8 watt Allen-Bradley carbon resistors used to monitor the temperature. The "plate thermometer," located at the top of the sample plate, was used to measure any temperature gradients in the vertical direction. It was wrapped with copper wire to improve thermal contact and varnished to the sample plate with GE 7031 varnish. The "beam thermometer" was suspended by its leads in the path of the electron beam next to the sample, and was used primarily as a qualitative measure of the heating seen by the sample during irradiation. It also served to measure temperature gradients during annealing. The "sample thermometer" was mounted directly below the sample in the same manner as the plate thermometer. The sample thermometer was monitored continuously, and its reading assumed to correspond to the sample temperature.

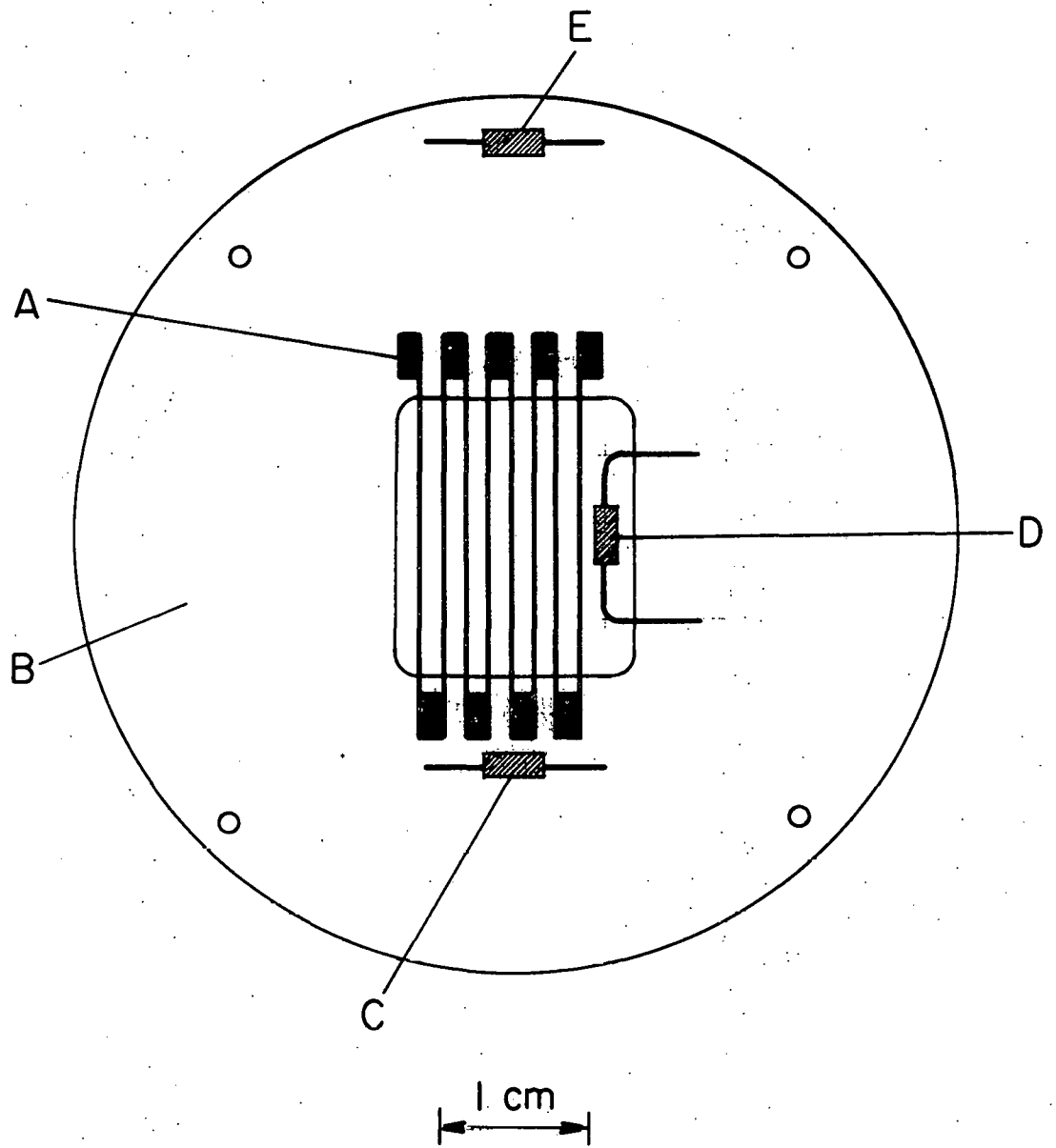
All three carbon thermometers were calibrated according to the empirical relation

$$\left[\frac{\log R}{T} \right]^{1/2} = A + B \log R \quad (\text{II-1})$$

where R is the resistance, T the temperature, and A and B adjustable fitting parameters. This fit was found to deviate from the measured relationship by 0.4% in the range 4-25 K for 10Ω 1/2 Allen-Bradley

Figure 7. Magnesium sample mounted on sample plate showing location of carbon resistance thermometers. All wiring excluded for clarity.

- (A) Sample
- (B) Sample mounting plate
- (C) Sample thermometer
- (D) Beam thermometer
- (E) Plate thermometer



resistors.^{17/} In the present case, A and B were determined by measuring R at T = 77.35 K and 4.215 K. The calibration was checked by measuring the vapor pressure above the liquid helium bath near the lambda point (2.174 K) and was found to agree to within 2%. The sample thermometer was re-calibrated after all of the irradiations were completed, undergoing a shift of less than 0.001 K from the original calibration between 1.3-20 K.

During irradiation, the sample temperature will rise due to the energy loss of the electron beam in the sample. The power dissipated in the sample due to this loss is given by

$$P = \frac{dE}{dx} \dot{\phi} V$$

where dE/dx is the stopping power for the electrons = 1.557 MeV cm²/g for 1.0 MeV electrons in magnesium,^{16/} $\dot{\phi}$ is the electron flux rate, and V is the sample volume. Using $\dot{\phi} = 2.68 \times 10^{11} \text{ e}^-/(\text{cm}^2 \text{ sec})$, the highest flux rate attained in this experiment, and the nominal dimensions of the irradiated region of the sample, $V = 0.27 \text{ cm} \times 0.011 \text{ cm} \times 13.97 \text{ cm} = 4.15 \times 10^{-3} \text{ cm}^3$, we find $P = 0.48 \times 10^{-3} \text{ watts}$. Similar calculations yield $12.37 \times 10^{-3} \text{ watts}$ for the power dissipated in the helium bath, $2.67 \times 10^{-3} \text{ watts}$ for the sample chamber windows, and approximately $3.87 \times 10^{-3} \text{ watts}$ for electrons stopped completely by the front plate of the sample chamber and, due to wide angle scattering, inside the sample chamber, giving a total heat dissipation in the sample chamber of about $19.5 \times 10^{-3} \text{ watts}$. The sample heating accounts for only 2.5% of this total.

The temperature difference between the center and the surface of a round wire with uniform heating is given by

$$\Delta T = \frac{1}{4\pi\kappa} \frac{P}{\ell}$$

where κ is the thermal conductivity and P/ℓ is the heating per unit length. Approximating the rectangular legs of the sample to be circular with $P/\ell = 3.44 \times 10^{-5}$ watts/cm from above and $\kappa = 1.95$ watts/(cm K),^{18/} we find $\Delta T = 1.4 \times 10^{-6}$ K. The temperature difference should be less for rectangular wires. The maximum heat flux across the surface of the sample was 4.52×10^{-4} watts/cm². Using the approximate curve for Kapitza resistance given by Harrison,^{19/} the Kapitza resistance of magnesium at 1.55 K can be estimated to be 3.2 K cm²/watt, a value in general agreement with other metals at this temperature.^{20,21/} The sample surface temperature is thus estimated to be 1.45×10^{-3} K warmer than the surrounding bath. Finally, in a superfluid helium capillary at 1.5 K, Keesom et al.^{22/} found that a heat flux of 0.233 watts/cm² applied at one end gave rise to a temperature gradient of 0.136×10^{-3} K/cm along the capillary. Using this value as a very conservative upper limit, we can estimate the maximum temperature difference between the sample thermometer and the center of the sample 1.5 cm away to be 2.04×10^{-4} K. Thus, the sample was expected to be at most 1.7×10^{-3} K warmer than the sample thermometer reading of 1.55 K during irradiation, well within the uncertainty associated with carbon resistance thermometry. As an experimental check, when 0.245 watts were dissipated in the sample heater, the sample temperature rose from 1.3 K to only 1.46 K.

During resistivity measurements, sample heating by the measuring current is given by the current times the potential. For the largest value of sample resistance in the high dose isochronal run, this amounted to 0.26×10^{-3} watts. The sample heating, together with heating due to the resistance of the copper current leads, raised the sample temperature by 0.03 K.

In conclusion, the highest sample temperature during irradiation or measuring was 1.65 K, which occurred when the needle valve was opened to fill the refrigerator. All irradiations were done at or below 1.55 K.

E. Resistivity Measurements

Standard four-point d.c. potentiometric techniques were used to measure the sample resistivity. The voltage across the sample (about 200 μ V) was measured with Rubicon #2768 6-dial potentiometer with a Leeds and Northrup #9838 nanovolt detector as a null detector; the net resolution was $\pm 0.01 \mu$ V. A Fluke 382A Current Calibrator was used to supply a measuring current of 1 ± 10^{-5} Amperes to the sample. The resulting uncertainty in the sample resistivity was $1.4 \times 10^{-13} \Omega\text{cm}$. All measurements were made with the sample immersed in superfluid helium below 1.35 K, where the thermal contribution to the sample resistivity was below the resolution of the measuring system.

The entire measuring system was battery operated and shielded both electromagnetically and from drafts to avoid a loss of resolution to thermal and electrical noise. In addition, the sample potential leads were twisted and contained in a continuous electrical shield from the cryostat to the measuring system.

Stable thermal e.m.f.'s (amounting to about $0.3 \mu\text{V}$) in the spot-welds, solder joints to the sample potential leads in the sample chamber, and due to cooling of the potential leads by helium gas were averaged out by reversing the measuring current to the sample, using a Rubicon #3565 Thermofree Reversing Key to reverse the input to the 6-dial.

F. Anneals

Two types of annealing experiments were used to study the recovery of the damage in the irradiated samples. In both cases, the temperature was raised by valving off the refrigerator pump and passing current through a heater wire (chromel A, nominal resistance of 50Ω) mounted on the sample plate. For anneals above 6 K, the heater was used to boil away all of the liquid in the sample chamber, then the refrigerator was evacuated to a pressure of below 10 mm Hg. The sample heater was then used to bring the sample plate to the desired temperature.

Isochronal anneals in steps of 0.25 K for holding times of five minutes were done to study the temperature dependence and kinetics of the recovery. The time to raise the sample from one temperature to the next was always less than five seconds. The cooling time after each anneal was less than one second for a decrease of several K.

Isothermal anneals were performed to study the time dependence of the recovery. Repeated anneals were done at the same temperature with a resistivity measurement at the base temperature between each anneal. This process was repeated at successively higher temperatures, moving from one temperature to the next after the time dependence was established for each temperature.

The temperature stability during annealing was poorest between 4.5-6.5 K for all anneals, due to the fact that the sample plate tended to rise to about 6.5 K with zero heat input once the liquid was gone. It was usually possible to hold the annealing temperature to within ± 0.1 K in this range. The stability was very much improved at higher temperatures; between 6.5-10.0 K the temperature was maintained to ± 0.004 K; between 10.0-14.0 K, to ± 0.005 K.

As a check on the annealing temperature as given by the sample thermometer, readings of the plate and beam thermometers were taken during a simulated anneal. For a sample thermometer temperature of 7.50 K, the plate thermometer read 7.47 K and the beam thermometer 7.46 K. For 12.5 K on the sample thermometer, the plate and beam thermometers both read 12.37 K. These small differences are well within the range which might be expected because of temperature gradients and differences in thermal contact to the sample plate.

III. EXPERIMENTAL RESULTS AND ANALYSIS

A. Damage Production

The damage production for several irradiations with 1.0 MeV electrons at 1.55 K in one sample is shown in Figure 8. The production rate decreases gradually up to about 3×10^{-10} Ωcm of damage. A straight line fit to the remaining damage production data using the method of least squares gave a production rate of $(3.57 \pm 0.03) \times 10^{-26}$ $\Omega\text{cm}/(e^- \text{cm}^2)$. The initial curvature of the production rate may result from deviations from Matthiessen's rule for very low defect concentrations^{23/} and/or from size effects in the resistivity.

The 1.0 MeV electrons striking the sample could transfer a maximum of 179 eV to a magnesium atom. The average energy transferred was about 26 eV. Since the threshold energy for atomic displacements in magnesium is about $10 \text{ eV}^{10/}$ and the sample thickness much less than the range of the electrons, a homogeneous distribution of isolated vacancy-interstitial pairs was expected due to irradiation. In addition, some small clusters of 2-3 interstitials may have been formed.

B. Isochronal Anneals

The isochronal recovery results following irradiations to three different initial defect concentrations in the same sample are shown in Figure 9. Figure 10 shows the derivative of the recovery with respect to temperature for these three runs. The sample was warmed to room temperature between runs, allowing all of the radiation-induced damage to anneal.

Figure 8. Change in resistivity as a function of integrated flux for magnesium irradiated at 1.55 K with 1.0 MeV electrons.

- - high dose isochronal irradiation
- - data from five other irradiations

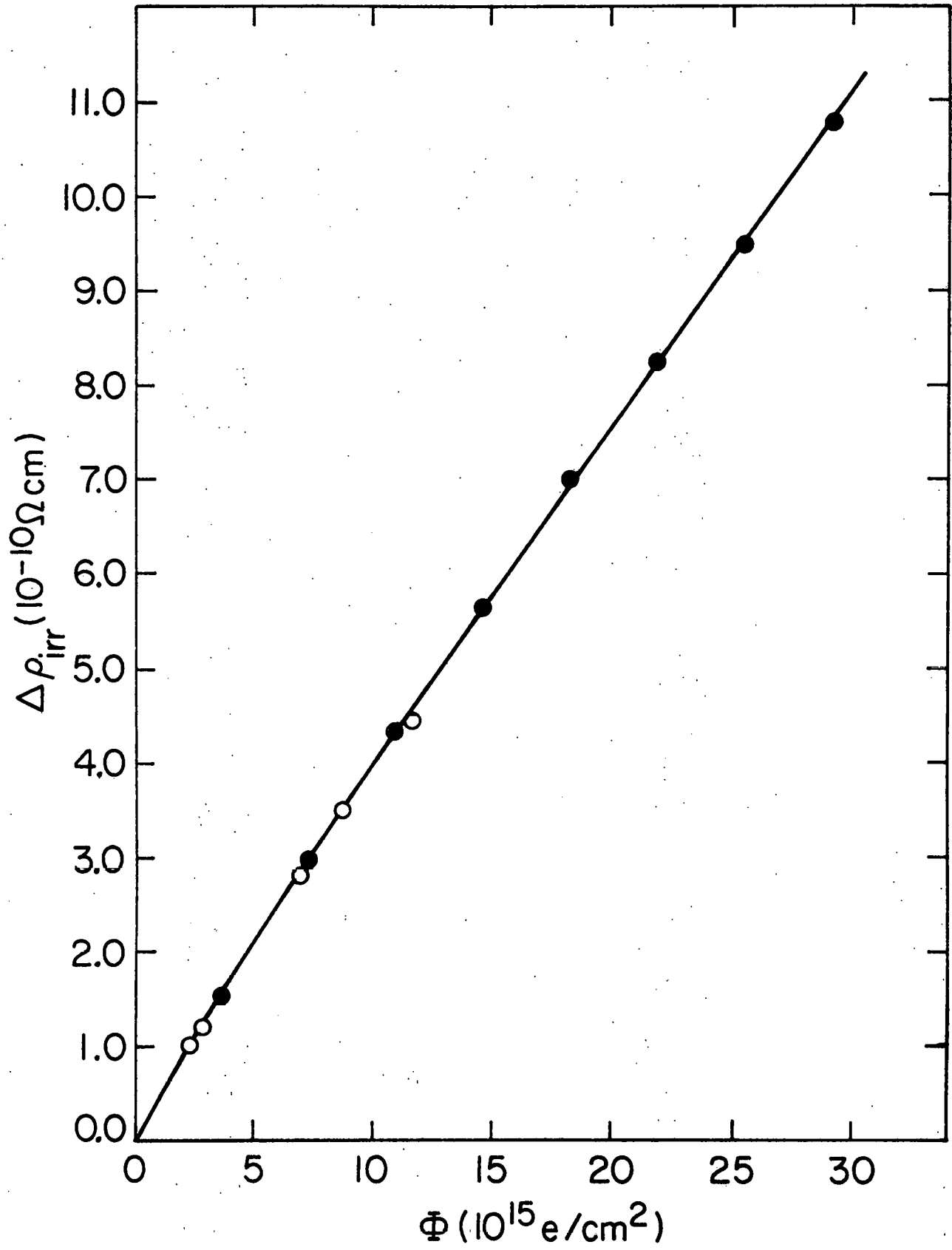


Figure 9. Isochronal recovery of electrical resistivity in one sample after 1.0 MeV irradiations at 1.55 K to three different doses. Sample annealed to room temperature between irradiations.

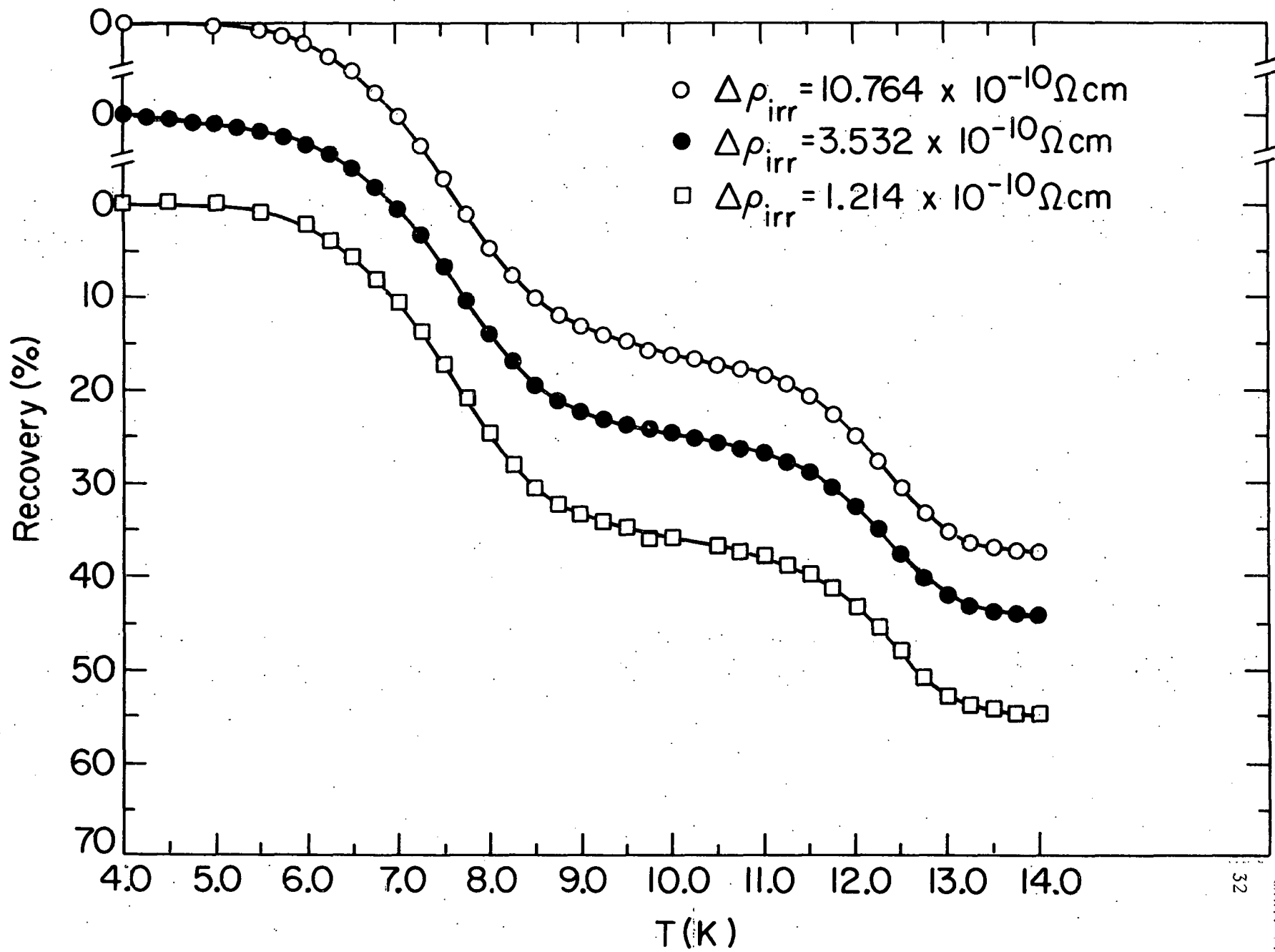
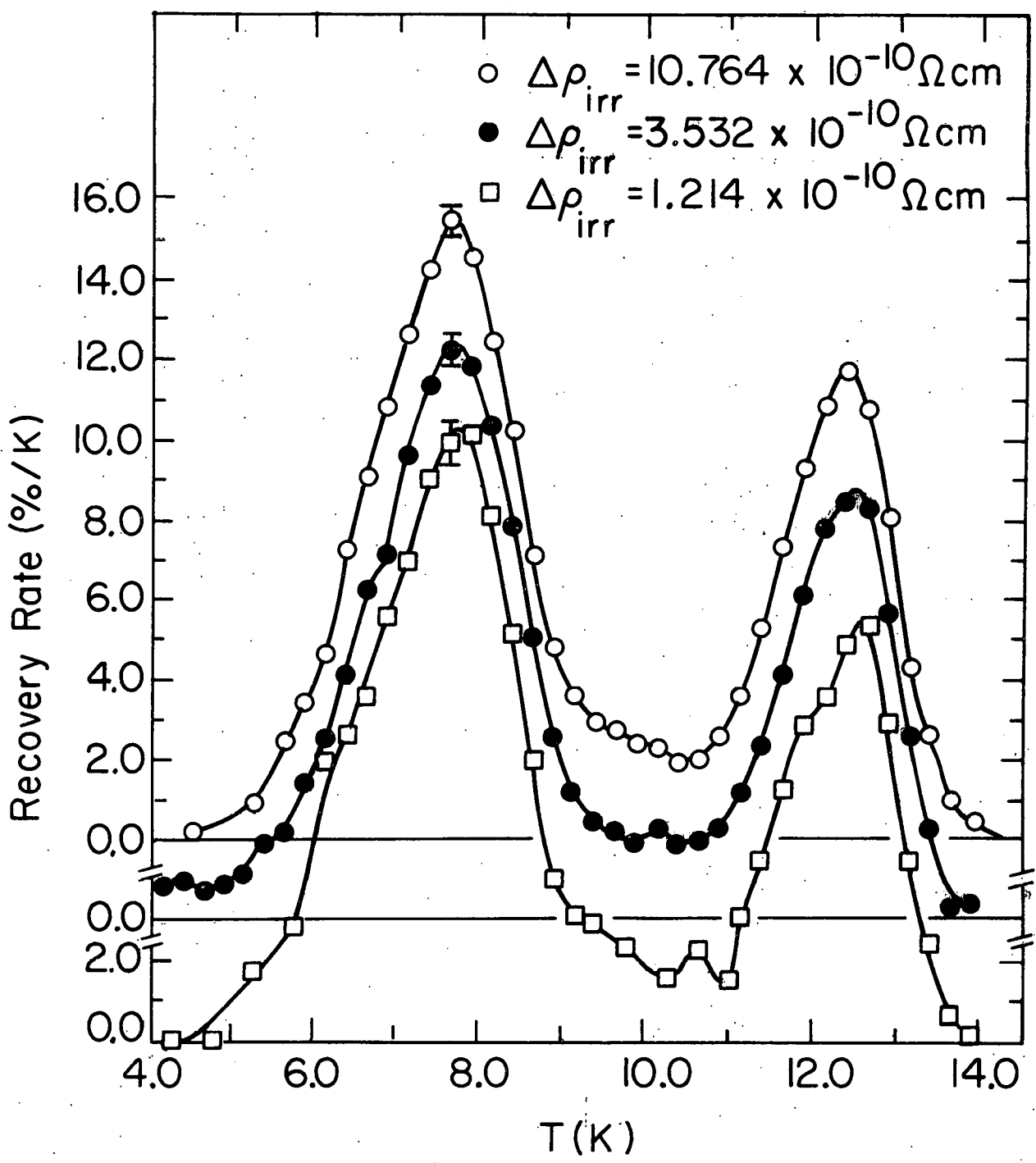


Figure 10. Differential isochronal recovery of the irradiations
of Figure 9.



The low temperature isochronal recovery in magnesium is characterized by two distinct substages. Substage I (4.5-9.5 K) is a fairly symmetric peak centered at 7.7 K with a peak width at half maximum of 2.15 K. About 34.5% of the total damage is recovered in substage I for all three irradiation doses. Substage II (10.5-14.0 K), centered at 12.50 K with a width of 1.55 K, shows evidence of substructure which changes with dose. The recovery in this substage increases from 17.5% for the low dose to 20% for the high dose. There is in addition some background annealing occurring between the two substages for which about 2% recovery is seen for all doses. No further annealing was observed up to 25 K. Also, no annealing was seen below substage I down to 1.55 K.

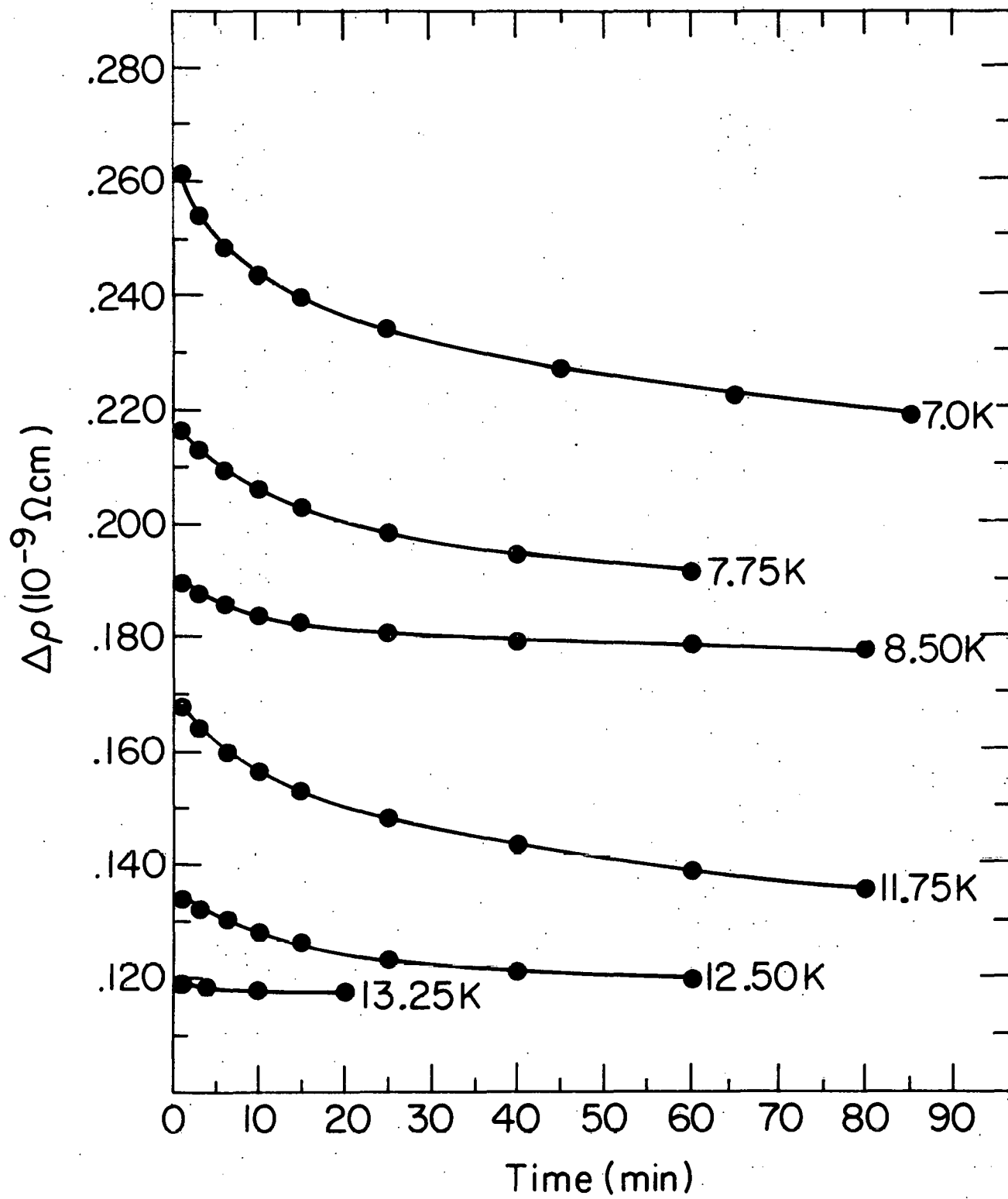
There is some shifting of both substages to lower temperatures with increasing dose, particularly for substage II, which is indicative of recovery other than the recombination of vacancy-interstitial close pairs. However, the magnitudes of the shifts are smaller than would be expected due to a simple second-order annealing process, as is observed for the I_E substage of the f.c.c. metals, or for a third-order process. Also, both substages are wider than would be expected for a single thermally-activated process^{1/} (see Appendix C).

C. Isothermal Anneals

The time dependence of the low temperature recovery was investigated in two isothermal annealing experiments. For isothermal run 1 (Figure 11), the total radiation-induced change in resistivity was $2.756 \times 10^{-10} \Omega\text{cm}$, and three isothermal anneals were made over the temperature range of each of the two low temperature substages. The total change

Figure 11. Isothermal recovery of electrical resistivity
after 1.0 MeV irradiation at 1.55 K.

$$\Delta\rho_{\text{irr}} = 2.756 \times 10^{-10} \text{ } \Omega\text{cm.}$$



for isothermal run 2 (Figure 12) was $3.506 \times 10^{-10} \Omega\text{cm}$; five isothermals were performed for substage I and three for substage II, with a short anneal in the temperature region of the background annealing.

Both isothermal run doses were comparable to that of the medium dose isochronal run. The relative recovery in each substage with respect to the total recovery was the same for the isothermal and medium dose isochronal runs. However, there was a total recovery of about 57.3% in both substages for the isothermal runs as compared to 54.5% for the isochronal run. The recovery in each substage was slightly enhanced for isothermal as opposed to isochronal annealing. In addition, the background annealing was not completely eliminated by the 40 minute isothermal at 9.42 K of isothermal run 2 as evidenced by the recovery in the subsequent 10 minute isothermal anneal at 10.42 K.

D. Activation Energy Determination

1. Slope Change Analysis. An attempt was made to calculate the activation energies for thermal annealing for the two substages from the isothermal annealing data using a slope change method suggested by Dibbert et al.^{24/} (see Appendix D). Such an analysis is valid regardless of the order of the recovery process, but will only yield a unique activation energy for recovery involving a single thermally-activated process. The results for both isothermal runs are shown in Table 1.

2. Primak Analysis. The annealing of kinetic processes distributed in activation energy was first considered by Primak.^{25/} His method of analysis has been applied to isothermal annealing data by numerous authors for both first-^{26/} and second-order^{27/} processes. (See Appendix E

Figure 12. Isothermal recovery of electrical resistivity
after 1.0 MeV irradiation at 1.55 K.

$$\Delta\rho_{\text{irr}} = 3.506 \times 10^{-10} \text{ } \Omega\text{cm.}$$

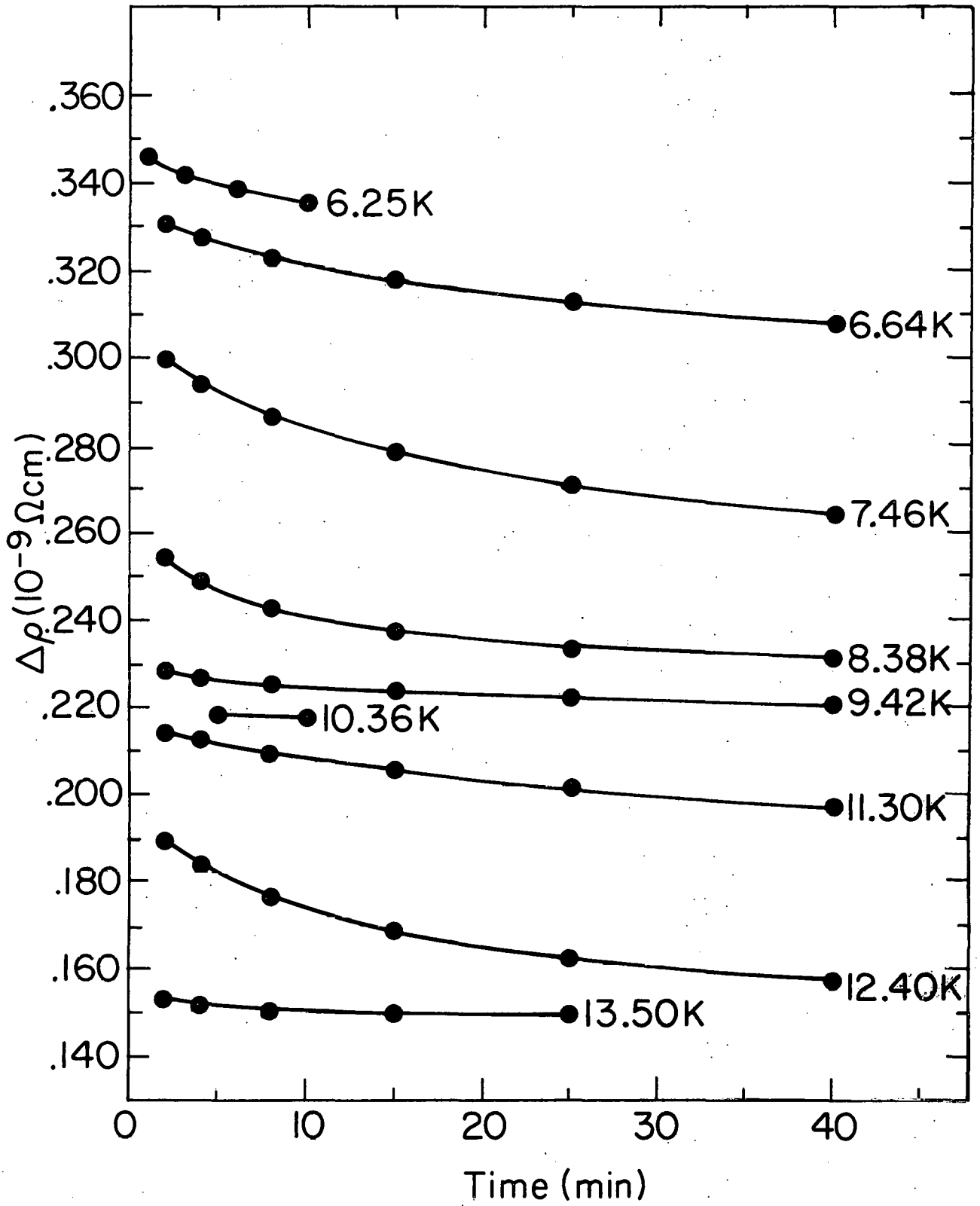


TABLE 1

Isothermal Run	Substage	Temperature (K)	E (eV)
1	I	7.00-7.50	0.0168 ± 0.001
		7.75-8.50	0.0177 ± 0.001
	II	11.75-12.50	0.0381 ± 0.002
2	I	6.25-6.64	0.0120 ± 0.002
		6.64-7.46	0.0156 ± 0.001
		7.46-8.38	0.0179 ± 0.001
		8.38-9.42	0.0227 ± 0.002
	II	11.30-12.40	0.0349 ± 0.002

for a detailed discussion of the analysis as applied to both orders.) In each case a resistivity density function is sought which can be plotted as a function of the activation energy.

For first-order processes the characteristic annealing function $\Theta(t, T)$ is defined as

$$\Theta(t, T_n) = \exp \left[-\Lambda t e^{-E/kT_n} \right] \quad (\text{III-1})$$

where t is the total time of annealing, T_n the temperature of the n^{th} anneal, Λ the frequency factor, E the activation energy, and k is Boltzman's constant. If $\rho(t_1, T_n)$ and $\rho(t_2, T_n)$ are two measured values of the remaining radiation-induced resistivity during the n^{th} anneal, then a first-order approximation of the resistivity density function can be written as

$$\begin{aligned} P_{01}(\bar{E}) &= \frac{\rho(t_1, T_n) - \rho(t_2, T_n)}{\int_0^{\infty} \left[\prod_{i=1}^{n-1} \Theta(t_i, T_i) \right] \left[\Theta(t_1, T_n) - \Theta(t_2, T_n) \right] dE} \\ &= \frac{\rho(t_1, T_n) - \rho(t_2, T_n)}{\int_0^{\infty} I_{n1} dE} \quad (\text{III-2}) \end{aligned}$$

\bar{E} is the average value of the activation energy associated with P_{01} and is given by

$$\bar{E} = \frac{\int_0^{\infty} E I_{n1} dE}{\int_0^{\infty} I_{n1} dE} \quad (\text{III-3})$$

The plotted activation energy spectrum of P_{01} vs \bar{E} evaluated from Equations (III-2) and (III-3) for some initial value of A will consist of several segments, one for each annealing temperature. The value of A is then varied successively until these segments fit together smoothly. The final smooth spectrum should give the distribution of activation energies for the temperature range covered by the series of isothermal anneals used in the calculations.

For second-order processes, the characteristic annealing function is

$$\theta(t, T_n) = \frac{A}{f} P_{02} t e^{-E/kT_n} \quad (\text{III-4})$$

Here f is the resistivity produced by 100% defects and P_{02} is the second-order resistivity density function, which is given by

$$P_{02}(\bar{E}) = \frac{\rho(t_1, T_n) - \rho(t_2, T_n)}{\int_0^{\infty} \left\{ \left[1 + \sum_{i=1}^{n-1} \theta(t_i, T_i) + \theta(t_1, T_n) \right]^{-1} - \left[1 + \sum_{i=1}^{n-1} \theta(t_i, T_i) + \theta(t_2, T_n) \right]^{-1} \right\} dE}$$

$$= \frac{\rho(t_1, T_n) - \rho(t_2, T_n)}{\int_0^{\infty} I_{n2} dE} \quad (\text{III 5})$$

As for the first order case,

$$\bar{E} = \frac{\int_0^{\infty} E I_{n2} dE}{\int_0^{\infty} I_{n2} dE} \quad (\text{III-6})$$

The activation energy spectrum is treated in the same manner as the first order case, except that here A/f rather than just A is varied.

The integrals for both cases were evaluated numerically on an LSI-11 computer using Simpson's Rule. Successive values of the integral were evaluated, each time doubling the number of intervals considered, until

$$\frac{(\int I_n dE)_i - (\int I_n dE)_{i-1}}{(\int I_n dE)_i} \leq 0.0001$$

For the second-order case it was also necessary to solve iteratively for P_{02} . Successive values were calculated until

$$\frac{P_{02}^k - P_{02}^{k-1}}{P_{02}^k} \leq 0.00001$$

The activation energy spectra for both first- and second-order Primak analyses appear in Figures 13 (run 1) and 14 (run 2) for the first substage and Figures 15 (run 1) and 16 (run 2) for the second substage.

3. Discussion. The activation energy results for the first substage indicate a spread of activation energies which is too wide to be the result of a single recovery process. The range for the slope change analysis agrees quite well with the Primak analysis for both first- and second-order kinetics for both isothermal runs. For first order, the frequency factor is a remarkably low $5 \times 10^7 \text{ sec}^{-1}$, good to within a factor

Figure 13. First- and second-order activation energy spectra
for substage I, isothermal run 1.

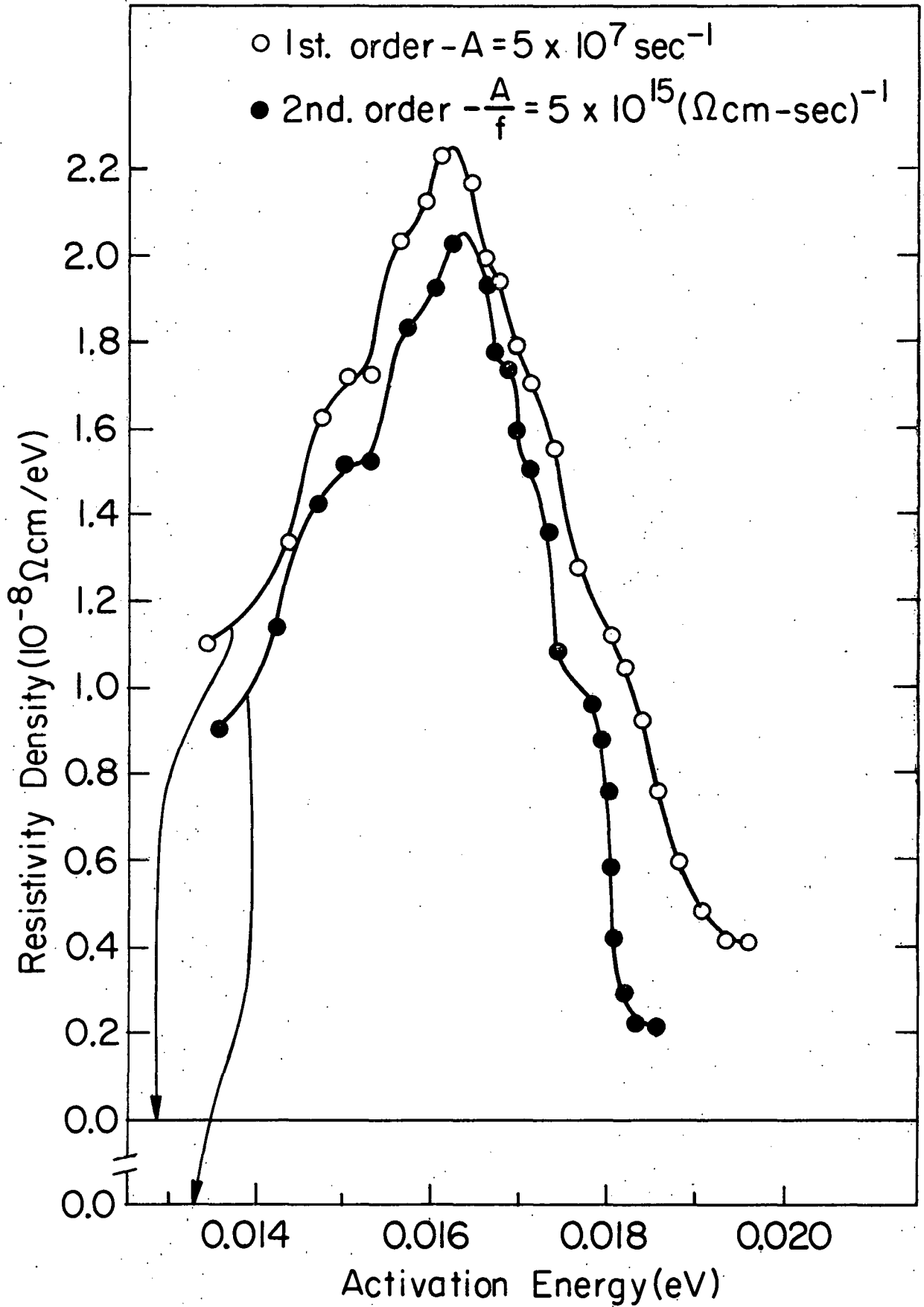


Figure 14. First- and second-order activation energy spectra
for substage I, isothermal run 2.

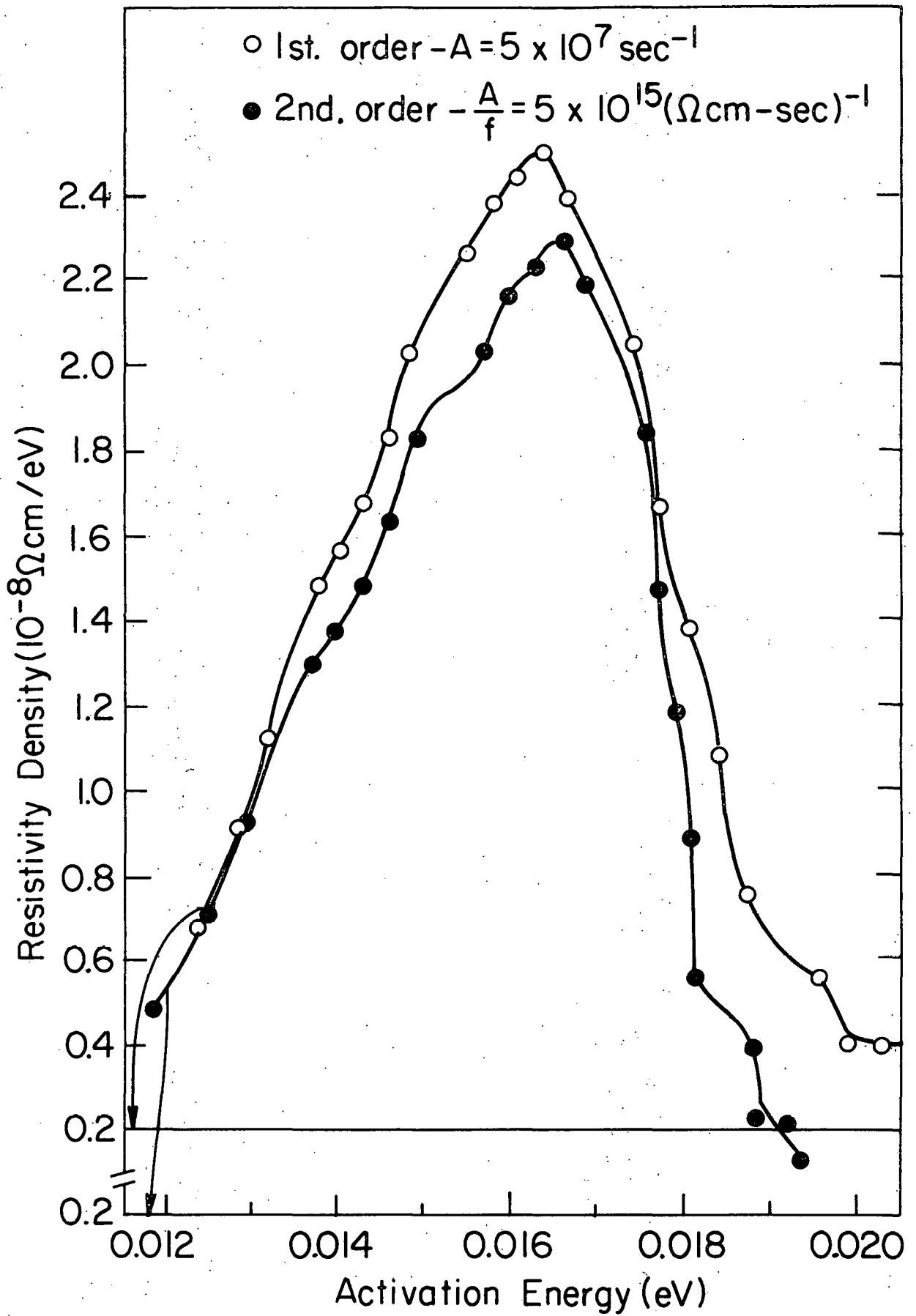


Figure 15. First- and second-order activation energy spectra
for substage II, isothermal run 1.

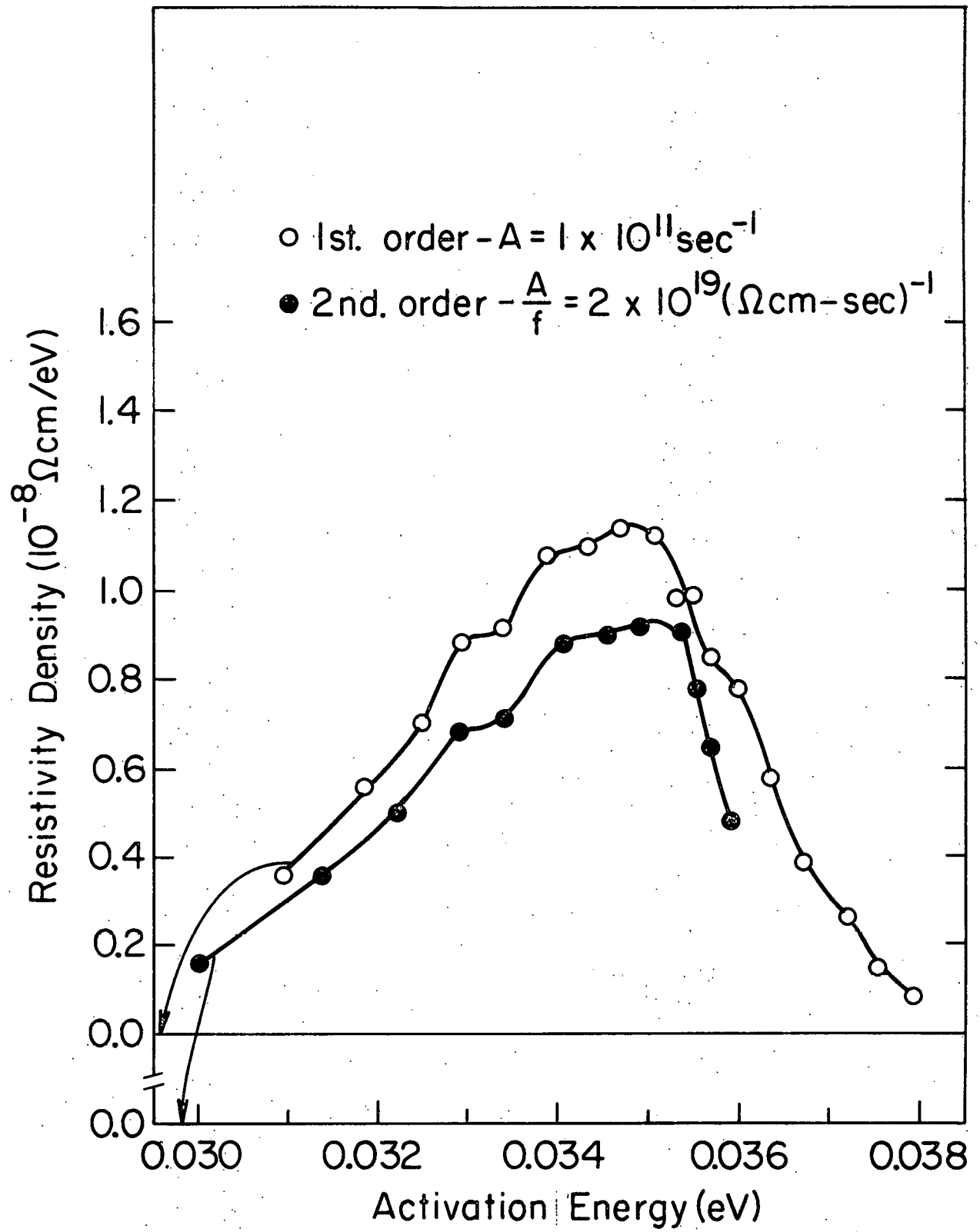
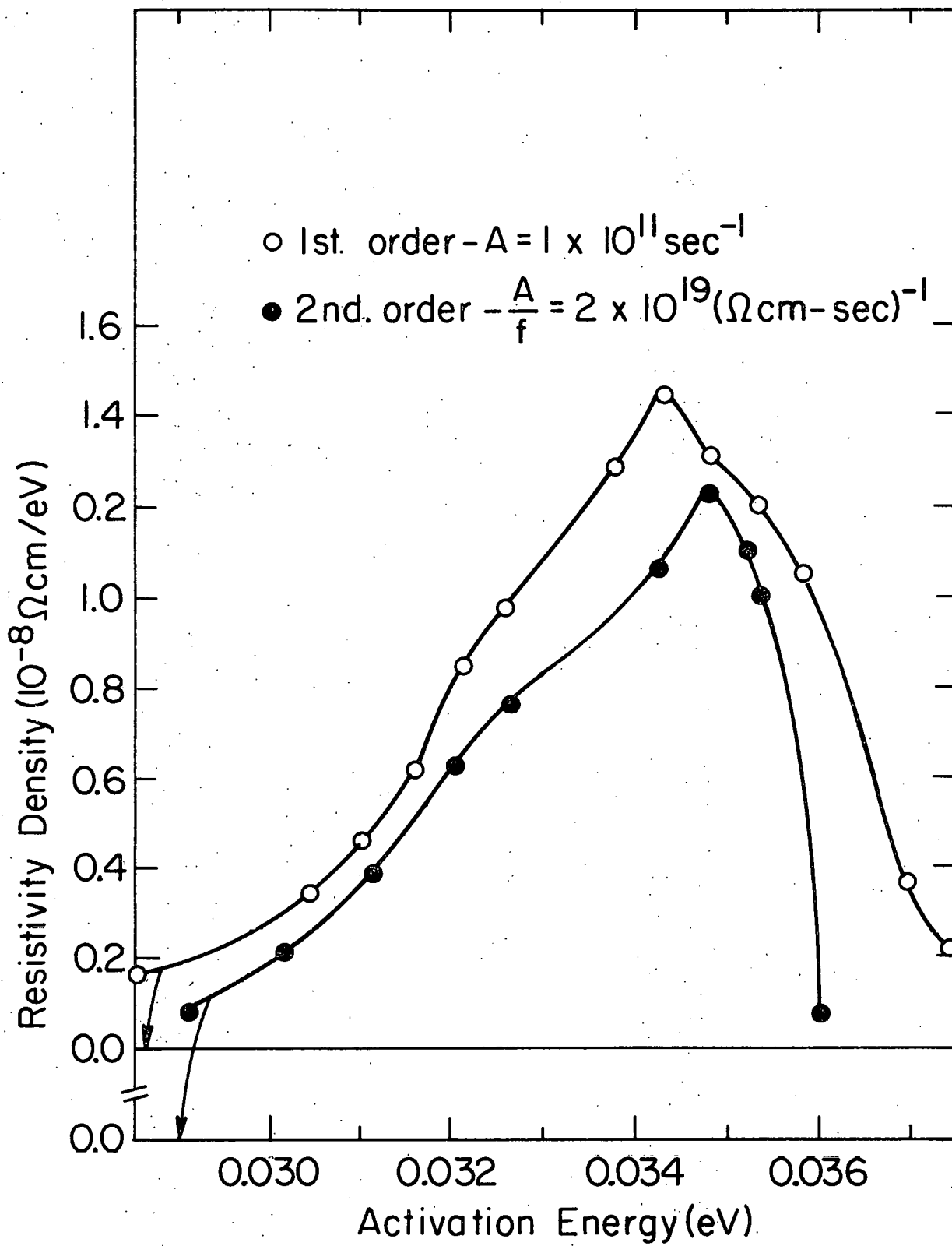


Figure 16. First- and second-order activation energy spectra for substage II, isothermal run 2.



of 2, as compared to typical values on the order of 10^{11} sec^{-1} for this temperature range.^{28/} For second-order, the value of the frequency factor depends on f ; using O'Neal and Chaplin's value of $4.5 \times 10^{-4} \Omega\text{cm}$ gives $A = 2.25 \times 10^{12} \text{ sec}^{-1}$, which seems somewhat high. For both orders, the uncertainty in A gives a shift in E of less than 0.001 eV. The activation energy spectra show strong evidence of substructure, with an average peak value of $0.0163 \pm 0.001 \text{ eV}$ for the first-order case. It is believed that this substage consists of several recovery processes too close in activation energy to be resolved individually.

The results for the second substage are not as definitive. The slope change and Primak analyses again yield similar values for the activation energy; however, the second-order analysis gives an unrealistically high frequency factor of $9 \times 10^{15} \text{ sec}^{-1}$. For the first-order case, $A = 10^{11} \text{ sec}^{-1}$. The breadth and substructure of the activation energy spectra suggest more than one recovery process, although the evidence is not as strong as for the first-order case. The average first-order peak value of the activation energy is $0.0345 \pm 0.001 \text{ eV}$.

E. Radiation Doping

Two radiation doping experiments were done to study the nature of the recovery in each of the two substages. For radiation doping, the sample is irradiated at low temperature, then annealed to above a recovery substage. The sample is then re-irradiated at low temperature and a standard annealing program is carried out. If the recovery involved in the initial anneal is comprised entirely of close-pair recombination, the doping will have no effect on the anneal following the second irradiation.

However, if long-range interstitial migration occurs in the doping substage, some of the interstitials involved will form clusters or be trapped at impurity atoms or dislocations, leaving an excess of vacancies available for interstitial annihilation during the second anneal. As a result, the recovery in the doped substage will be enhanced.

For doping run 1, the sample was irradiated to a total resistivity change of $6.471 \times 10^{-10} \Omega\text{cm}$, then warmed to 10.5 K for 60 minutes; 43% of the damage was recovered. The second irradiation was made to an additional resistivity increment of $3.086 \times 10^{-10} \Omega\text{cm}$, following which a standard isochronal annealing program was implemented. The results appear in Figure 17. The "recovery as measured" data correspond to the measured recovery of the total damage of the two irradiations less the 43% recovery from the 10.5 K anneal between irradiations. The adjusted data were evaluated for the relative equivalent amount of damage in each of the two substages. For the first substage this was $3.086 \times 10^{-10} \Omega\text{cm}$ since the substage I recovery from the first irradiation was already completed during the 10.5 K anneal. For the second substage the equivalent total damage was taken to be $9.557 \times 10^{-10} \Omega\text{cm}$; this assumes that the annealing in substage II is independent of the annealing in substage I.

The first irradiation for doping run 2 was to $6.417 \times 10^{-10} \Omega\text{cm}$, followed by a 60 minute anneal at 16 K for which 59% recovery occurred. The second irradiation was to an additional resistivity change of $3.160 \times 10^{-10} \Omega\text{cm}$, which was the value used in analyzing the recovery for this run. The isochronal recovery of doping run 2 is shown in Figure 18.

Figure 17. Isochronal recovery of electrical resistivity after radiation doping run 1. The upper curve gives the actual recovery as measured; the lower curve gives the recovery for each peak adjusted to the amount of doping (see text).

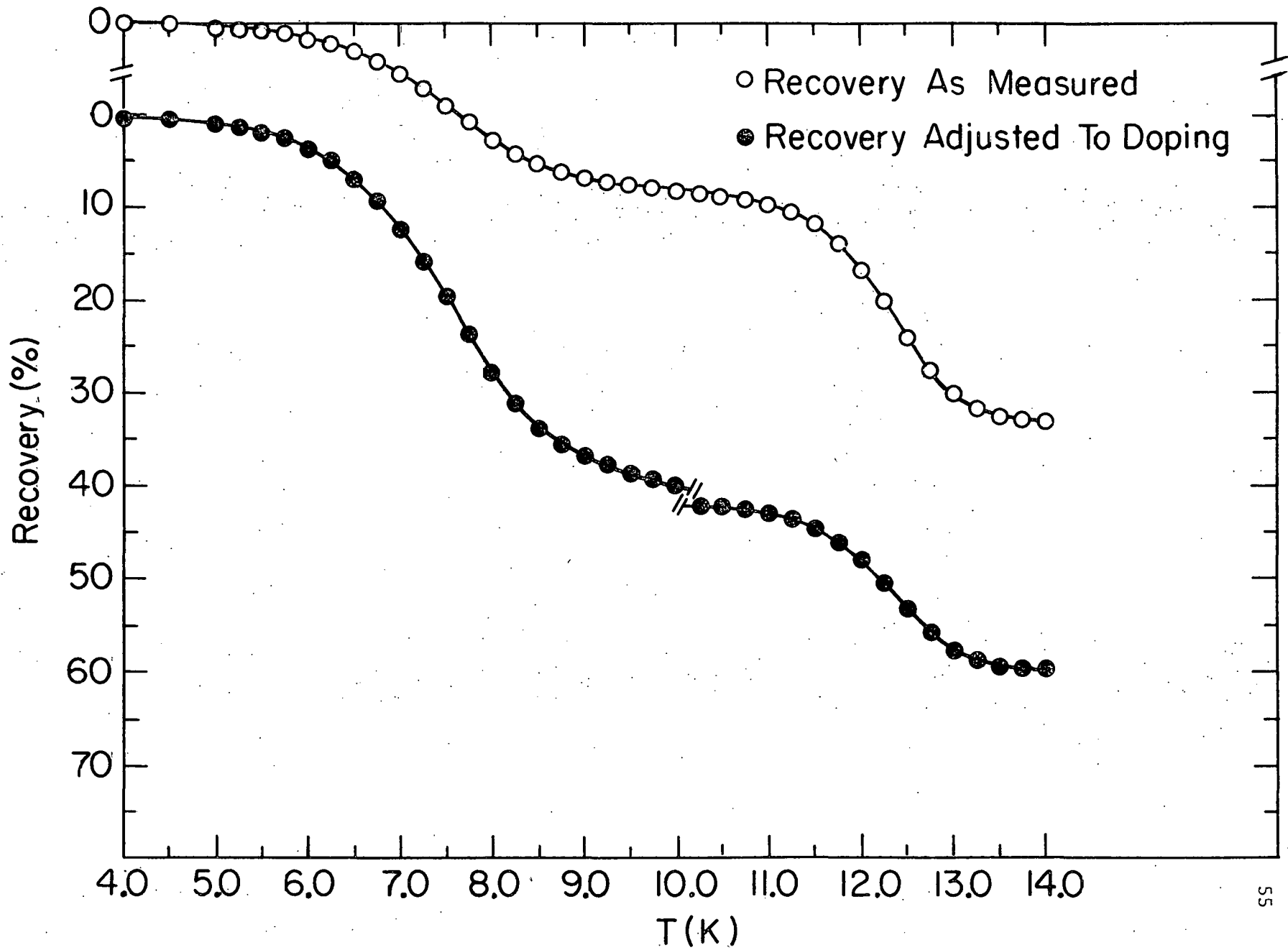


Figure 18. Isochronal recovery of electrical resistivity
after radiation doping run 2.

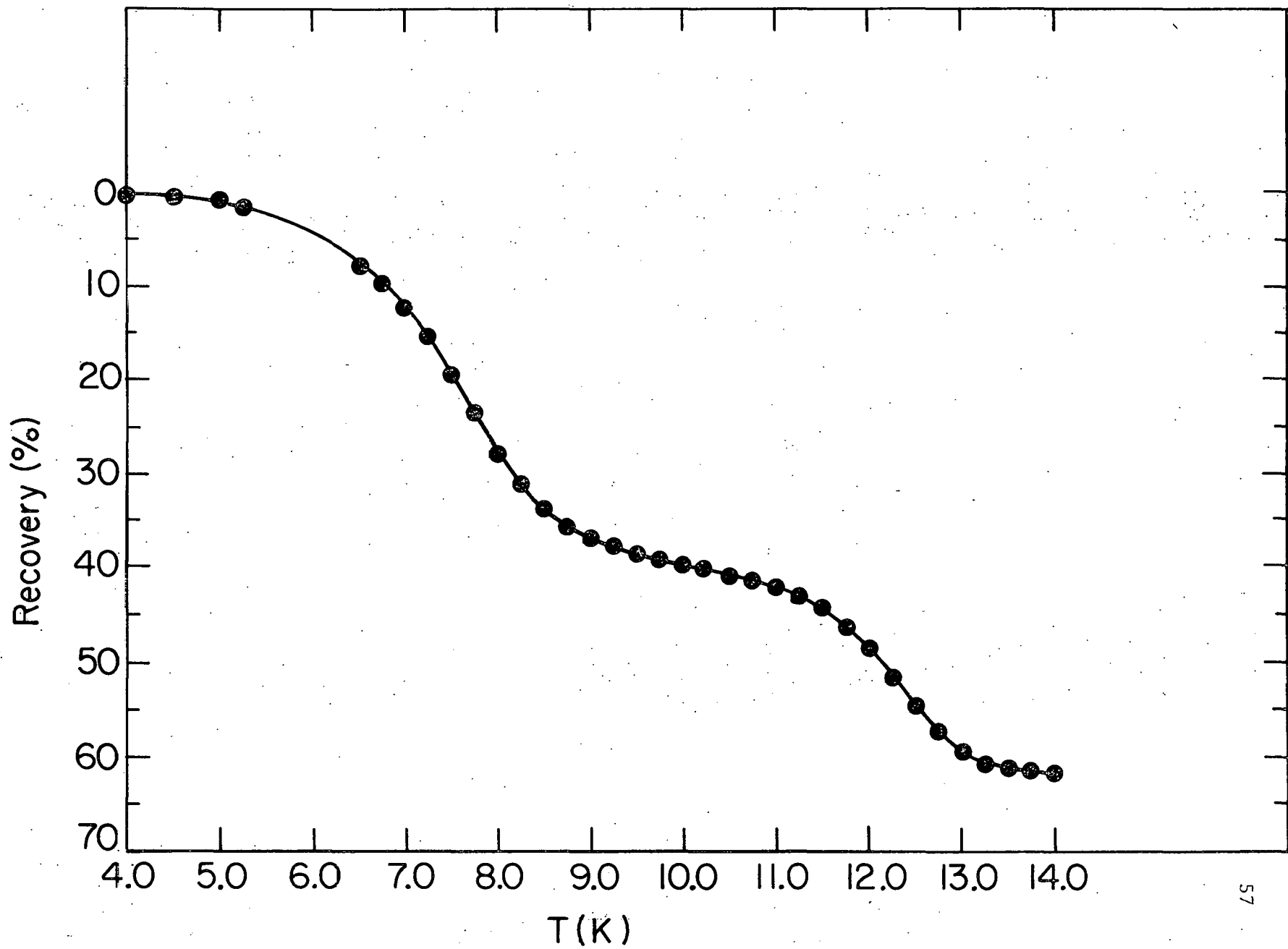


Figure 19 shows the differential recovery vs temperature for both doping runs; the adjusted data for run 1 has been plotted. The apparent shoulder on the low temperature side of substage I for the run 2 data is the result of a temperature control problem during this portion of the anneal. The remainder of the anneal should not have been affected. The results for the doping run recoveries are summarized in Table 2, along with the results for the three isochronal runs.

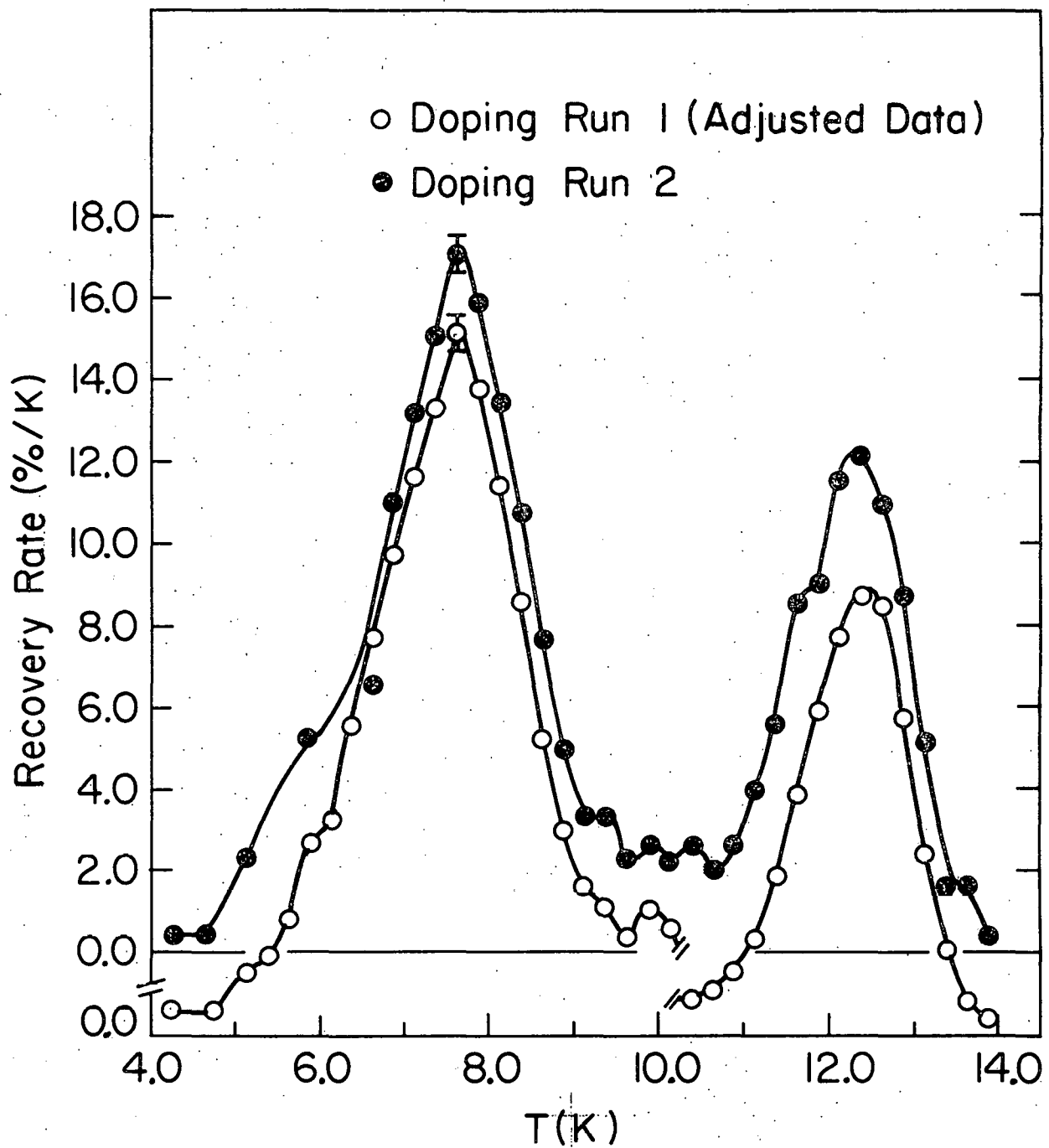
TABLE 2

Irradiation Run	Total Recovery	
	Substage I	Substage II
Low Dose Isochronal	34.2%	17.5%
Medium Dose Isochronal	34.4%	18.5%
High Dose Isochronal	34.9%	20.1%
Doping Run 1	38.6%	17.2%
Doping Run 2	38.6%	20.7%

The first substage recovery is clearly enhanced over the isochronal run recovery. The widths, relative magnitudes, and locations of the two doping run peaks are in very good agreement; the location and shape of the peaks are more like those of the high dose rather than the medium dose isochronal run, although the damage was slightly less than that for the medium dose run.

The adjusted second substage recovery for doping run 1 is less than was expected since the equivalent damage was nearly that of the high dose isochronal run. The peak shape, location, and magnitude are very similar

Figure 19. Differential isochronal recovery of radiation doping runs 1 and 2 (Figures 17 and 18). The adjusted data for doping run 1 has been plotted.



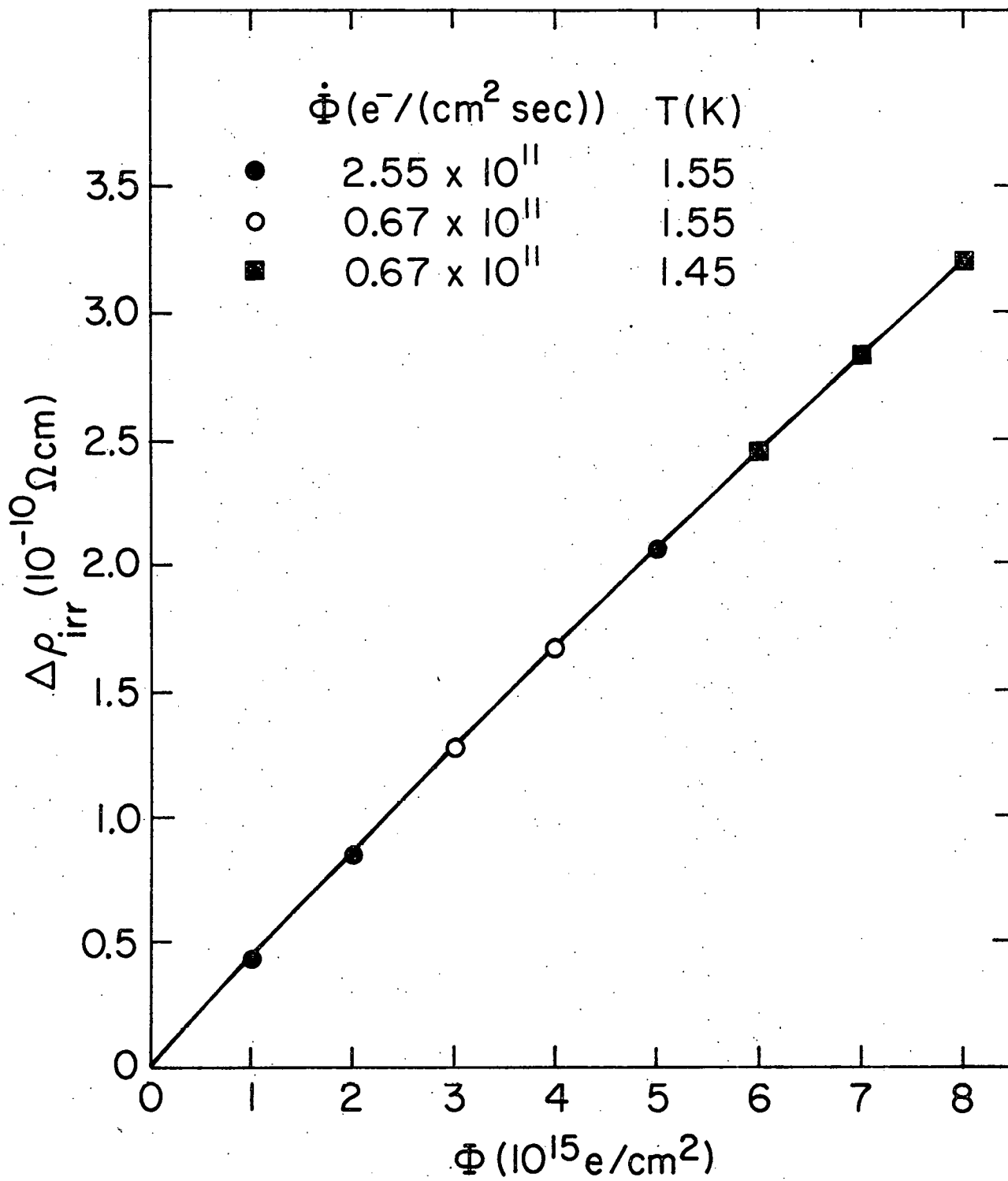
to those of the medium dose isochronal run. It is possible that some substage II recovery occurred during the one hour 10.5 K anneal between irradiations. For doping run 2, however, the recovery is enhanced over the isochronal run recovery. The peak location is shifted near that for the high dose isochronal run, and a low temperature side shoulder has become evident.

In summation, radiation doping results in an enhancement of the correspondingly doped substage recovery and an apparent shift of the substage location to lower temperatures analagous to the shift normally observed for concentration-dependent recovery involving long-range migration of the interstitial.

F. Other Results

To investigate the possibility of thermal annealing occurring at or near the irradiation temperature of 1.55 K a two part experiment was carried out (see Figure 20). In the first part, the electron beam flux rate was varied at constant temperature. Two damage production points were measured after irradiation at 1.55 K with a flux rate of 2.55×10^{11} $e^-/(\text{cm}^2 \text{ sec})$. The flux rate was then decreased by 74% to 0.67×10^{11} $e^-/(\text{cm}^2 \text{ sec})$; to maintain the same irradiation temperature for this decrease in beam heating, the cooling power of the refrigerator was reduced by throttling down the mechanical pump used to pump on the liquid helium. Two more production points were taken at the reduced flux rate. A fifth production point was then taken at the original higher flux rate with the pump valved open again. All points were measured in flux increments of 10^{15} e^-/cm^2 .

Figure 20. Change in resistivity as a function of integrated flux for different flux rates at two different irradiation temperatures.



Gwozdz and Koehler^{4/} performed an experiment similar to the one outlined above for 1.7 K irradiations of gold, in which thermal annealing is believed to occur below 2 K. They found that the damage production rate was higher for higher flux rates. By contrast, the results for the present experiment show a continuous production rate regardless of flux rate.

For the second part of the experiment, three additional damage production points were measured for irradiation at 1.45 K with the lower flux rate given above. Care was taken to only crack the needle valve open during remote filling of the refrigerator to keep the sample temperature below the irradiation temperature.

As can be seen from Figure 20, the final three production points fall on the same curve as the points from part one of the experiment. In addition, all eight production points for this experiment can be fitted to the damage production curve of Figure 8. From these results and the previously discussed isochronal annealing results, there is no evidence for thermal annealing in magnesium between 1.45-4.5 K.

G. Summary and Comparison to Other Experiments

The damage production rate for 1.0 MeV electron irradiations of magnesium at 1.55 K is found to be linear with increasing electron flux. No evidence for thermal annealing near the irradiation temperature was found; in fact, it was demonstrated experimentally that such annealing does not occur.

The low temperature recovery in magnesium following 1.0 MeV electron irradiations at 1.55 K consists of two major substages. Evidence for

multiple recovery processes in both substages is provided by the substage widths, their ranges of activation energies, and the small magnitude of the temperature shift of each substage peak with changing initial defect concentration. The lack of dose-dependence of each substage as a whole and the spread of activation energies suggest that at least the low temperature portion of each substage is due to close-pair and/or correlated long-range recovery. The dose-dependent shifts of the actual substage peaks and, more significantly, the recovery enhancement in both substages due to radiation doping indicate that some form of uncorrelated long-range recovery occurs in the high temperature region of each substage. Thus, it seems that each of the two low temperature recovery substages consists of a combination of correlated (close-pair and/or long-range) and uncorrelated recovery.

There are some significant differences between the two substages. The first substage is 40% broader, exhibits a less pronounced dose-dependent peak shift, and has a frequency factor at least three orders of magnitude smaller than the second. Substage I accounts for almost 2/3 of the low temperature recovery, as compared to about 1/3 in substage II; however, the total recovery in substage II increases with dose, while that in substage I remains about the same. And finally, the recovery processes in the second substage seem to be somewhat dependent upon those in the first as evidenced by the combined results of the two radiation doping experiments. The enhancement of the first substage recovery was the same whether one or both substages were doped; however, for doping of the first substage only, the enhancement in substage I was accompanied by a decrease

in the second substage recovery compared to what was expected based upon the calculated equivalent damage. The end product of the long-range recovery in substage I or the recovery process itself acts to suppress the recovery in substage II.

The results of O'Neal and Chaplin (OC)^{10/} for 0.4 MeV electron irradiations of polycrystalline magnesium, while qualitatively similar, differ from those of the present work in several respects. OC also found two low temperature recovery substages, but their lowest temperature substage was asymmetrical (a peak with a high temperature shoulder). In addition, the amount of recovery in each of their substages and for the low temperature region as a whole differed from that of the present work, as shown in Table 3. (OC' refers to earlier work by O'Neal and Chaplin for irradiations with 0.3 MeV electrons.^{29/}) And finally, OC observed no dose-dependence in either substage for isochronal anneals following irradiations to total resistivity changes of $4.3 \times 10^{-10} \Omega\text{cm}$ and $18.1 \times 10^{-10} \Omega\text{cm}$.

TABLE 3

Experiment	e ⁻ energy (MeV)	$\Delta\rho_{\text{irr}}$ ($10^{-10} \Omega\text{cm}$)	Recovery		
			Substage I	Substage II	Total
This Work	1.0	10.764	34.9%	20.1%	58%
OC	0.4	9.08	37%	34%	73%
OC'	0.3	8.36	43%	37%	82%

The differences outlined above can be explained, for the most part, in light of two basic experimental differences between the present work

and that of OC. First, OC performed their irradiations around 5 K, for which they saw clear evidence of thermal annealing during irradiation. Their damage production rate decreased with increasing electron flux, and when they lowered their irradiation temperature by decreasing the electron flux rate, they observed a marked increase in the production rate. Further, the production rate of $3.57 \times 10^{-26} \Omega\text{cm}/(e^- \text{cm}^2)$ found in the present investigation for 1.0 MeV irradiations is 46% higher than predicted by an extrapolation of OC's values for irradiations between 0.125-0.4 MeV. Thus, the substage I recovery seen by OC and given in Table 3 is less than the intrinsic recovery for this substage by some unknown quantity dependent upon the amount of thermal annealing which occurred during irradiation.

The second basic difference concerns the electron energies used for irradiation. For f.c.c. metals, results for copper,^{30/} platinum,^{24/} and aluminum^{31/} indicate that increasing the energy of the incident electrons tends to decrease the population of the close-pair substages and increase that of the long-range migration substages by increasing the separation between the interstitial and its vacancy. As a result, since free long-range interstitial migration involves trapping of the interstitials and interstitial clustering in addition to recovery, the amount of defect retention above stage I generally increases with increasing electron energies. For the two experiments under consideration here, the population shift from close-pair to long-range configurations would explain the dissimilarity in substage I peak shapes, since OC would observe more close-pair recovery, giving an increased low temperature recovery sub-peak. Also, the increased defect retention for higher electron

energies explains the disparity in the substage and total recovery values, particularly in light of the above-mentioned conclusion that OC only saw some fraction of the intrinsic substage I recovery. This latter explanation is illustrated by the OC' results in Table 3, where the 0.3 MeV data exhibit recovery increases for both substages over the 0.4 MeV data.

The absence of evidence for dose-dependence in the OC study is probably due to the levels of defect concentrations chosen for their investigation. For sufficiently high concentrations, the f.c.c. substage E shifts so low in temperature that it becomes completely lost in substage D. In the present work, the peak shifts between the medium dose ($3.532 \times 10^{-10} \Omega\text{cm}$) and high dose ($10.764 \times 10^{-10} \Omega\text{cm}$) isochronal runs are minimal, and it was found necessary to drop to a low dose of $1.214 \times 10^{-10} \Omega\text{cm}$ to verify that some shifting was taking place. Since the OC low dose was higher than the present medium dose, and OC had a smaller relative population for uncorrelated recovery as discussed above, it is unlikely that they would have observed any significant shifting of either substage peak with dose.

The Schönfeld and Ehrhart (SE)^{11/} diffuse x-ray scattering studies for 3.0 MeV irradiations of magnesium single crystals provide several useful insights. They irradiated to total resistivity increments of 82-232 $\times 10^{-9} \Omega\text{cm}$, and observed small clusters of 2-3 interstitials following irradiation which had larger displacement fields in the basal plane than along the c axis. The cluster size was observed to increase during thermal annealing.

A question to be addressed is why SE saw clusters rather than single interstitials prior to thermal annealing. It is possible that

their irradiation temperature (near 5 K) was high enough that free migration of the interstitial was occurring during irradiation. However, in similar studies of cadmium and gold,^{32/} for which free interstitial migration is suspected below the irradiation temperatures used, the cluster size after irradiation was found to increase with dose. No such dose-dependence was seen by SE for magnesium. Thus, it seems more likely that the clustering in magnesium was due to a combination of radiation-induced diffusion and the influence of collision sequences, particularly in view of the rather high incident electron energy used (maximum lattice recoil energy of greater than 1000 eV!). As evidence, Ehrhart and Schlagheck^{33/} found for copper that high concentrations of defects (≥ 600 ppm) led to cluster formation during irradiation. Since the concentration for the temperature of free migration recovery to merge with correlated recovery has been shown in the present experiment to be quite small (~ 2 ppm as compared to ~ 50 ppm in copper), it is possible that the defect concentrations used by SE (180-500 ppm) were high enough to encourage cluster growth.

SE's observation that the long-range displacement field of the clusters was greater in the basal plane than along the c axis offers some information regarding the possible configuration of the interstitial in magnesium. In zinc, Ehrhart and Schönfeld found the displacement field to be greater along the c axis both for single interstitials^{9/} and for clusters of interstitials following thermal annealing.^{34/} Applying the inverse, the single interstitial in magnesium might be expected to lie more along the basal plane than along the c axis. Finally, the cluster size growth during thermal annealing, coupled with the above arguments

against free interstitial migration during irradiation, provides further support for free long-range migration of the interstitial in the low temperature recovery substages of magnesium.

IV. THEORETICAL MODEL FOR RECOVERY

A. Interstitial Model Calculations

1. Procedure. In order to develop an atomic model for the recovery processes observed in this investigation, it was first necessary to try to determine the configuration of the interstitial in magnesium. Since bulk measurements such as electrical resistivity yield no experimental atomic information and no experiments which do provide such information have been done for single interstitials in magnesium, theoretical calculations similar to those first used to determine the structure of the interstitial in f.c.c. and b.c.c. crystals were carried out. (For a review of the f.c.c. and b.c.c. calculations, see references 35-37.)

The basic procedure used can be outlined as follows. First, a suitable interatomic potential must be chosen; the Born-Mayer and Morse potentials have traditionally been the most popular choices for f.c.c. and b.c.c. materials. The unknown parameters in the potential are determined by fitting the potential to various known (calculated or, preferably, experimental) properties of the material being considered, such as the lattice parameter and the elastic constants. An interstitial atom is then "placed" into the lattice in some likely configuration, generally determined based upon lattice symmetry considerations, and the surrounding atoms are allowed to relax away from the interstitial. Finally, the energy difference between the normal perfect lattice and the relaxed lattice with the interstitial is calculated using the fitted potential. The amount of relaxation of the neighboring atoms and, in the case of a

split "dumbbell" structure, the separation between the two dumbbell atoms are then varied until an energy minimum is attained, which is taken to be the formation energy of the interstitial under consideration. The process is repeated for all likely interstitial structures; the one with the lowest formation energy is expected to be the actual interstitial configuration.

2. Potential. For the purpose of the present calculations, a Morse potential was chosen of the form

$$U(r) = D \left[e^{-2\alpha(r-R_0)} - 2e^{-\alpha(r-R_0)} \right]$$

fitted to experimental values of the lattice parameter ($a = 3.1926 \text{ \AA}^{\circ 38/}$), the vacancy formation energy ($E_F^V = 0.79 \text{ eV}^{\circ 12/}$), and the bulk modulus ($\kappa = 0.3689 \times 10^{12} \text{ dynes/cm}^2 \text{ }^{\circ 39/}$). For the vacancy formation energy, the 12 nearest neighbor (NN) and 6 next nearest neighbor atoms were considered, allowing no relaxation around the vacancy. The defining equation for the bulk modulus was used,

$$\kappa = V \frac{\partial^2 E}{\partial V^2}$$

where V is the volume and E the energy of the lattice. Finally, the equilibrium condition was applied,

$$\left. \frac{\partial U}{\partial r} \right|_{r=a} = 0$$

As a simplifying assumption in this and all further calculations, the magnesium lattice was taken to be ideally close-packed with $c = \sqrt{8/3} a$. The fitting procedure resulted in a transcendental equation which was solved numerically by iteration, giving $D = 0.1194 \text{ eV}$, $\alpha = 1.696 \text{ \AA}^{-1}$, and $R_0 = 3.231 \text{ \AA}$.

3. Configurations. Calculations were made for the four most likely interstitial configurations for hexagonal metals given by Ehrhart and Schönfeld^{9/} (see Figure 21). For the split dumbbell along the c axis (H_c) and octahedral (O) configurations, the six atoms forming triangles immediately above and below the interstitial were allowed to relax. For the tetrahedral (T) configuration, relaxations of the three atoms below and one above the interstitial were allowed. In all three cases, the 12 NN of the interstitial (both dumbbell atoms for H_c) and the 12 NN of each of the relaxed atoms were considered for calculating the configurational energy.

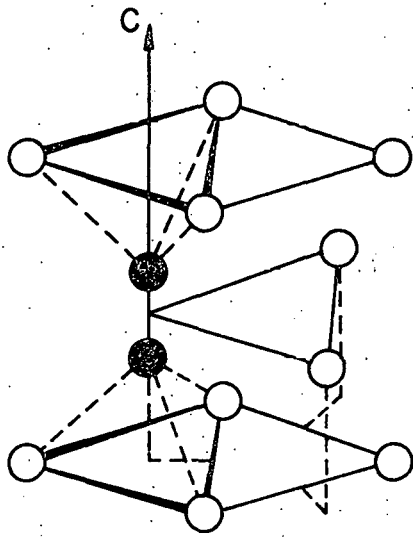
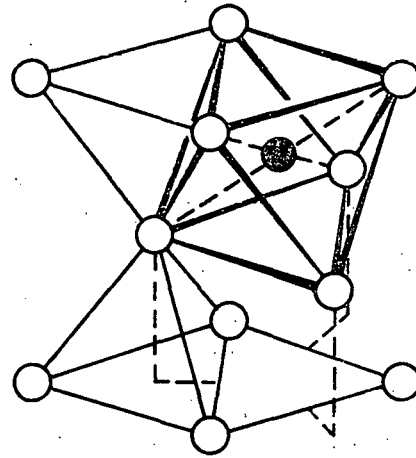
A different approach was used for the crowdion (C) configuration using the Frenkel-Kontorova model^{40/} based on a method due to Koehler.^{41/} For the contribution to the energy of atoms along the close-packed row of C, a "spring constant" β is determined for small displacements of atoms along the row. For atoms not on the row, the energy contribution V_0 is calculated in the same manner as discussed above for the other configurations. The two contributions are used to calculate a dimensionless parameter H,

$$H = \frac{\pi^2 V_0}{\beta a^2}$$

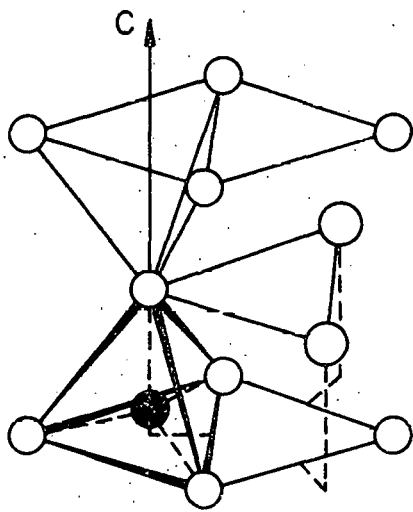
where a is the lattice parameter, from which the interstitial formation energy E_F^I may be evaluated. In the present work, a value of H was calculated for magnesium and E_F^I determined by quadratic interpolation from values given by Koehler.

The results of all calculations appear in Table 4. It should be noted that these values are not expected to represent accurate values for

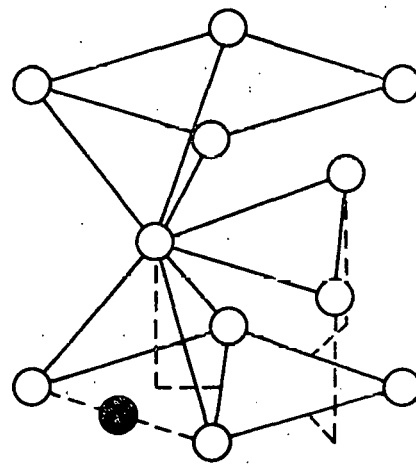
Figure 21. Single interstitial configurations considered for interstitial formation energy calculations.

dumbbell (H_C)

octahedral (O)



tetrahedral (T)



crowdion (C)

TABLE 4

Configuration	# atoms relaxed	# atoms considered	E_F^I (eV)
H_C	6	84	3.77
O	6	72	3.48
T	4	56	4.41
C	-	-	4.84

the interstitial formation energy; to achieve such accuracy would require many more relaxations than have been considered here. However, these calculations should reflect the relative magnitudes of E_F^I for the interstitial configurations studied.

It is clear from Table 4 that the T and C structures can be rejected. The O configuration has the lowest energy, with H_C about 8% higher. It would be difficult solely from these calculations to select either of these last two as the preferred structure. However, taking into account SE's scattering results for small clusters, O seems the more likely choice.

As was discovered for f.c.c. metals, not all potentials will give the same interstitial configuration as being lowest in energy;^{37/} models must ultimately be evaluated according to their agreement with experiment. Tome, Monti, and Savino^{42/} have investigated the O and T structures in magnesium with a potential consisting of a set of cubic functions continuous in different ranges, with their first and second derivatives matched at the boundaries. They found O to be unstable, moving to the T structure. Sahu, Srinivasan, and Krishan^{43/} have studied the single interstitial in magnesium using the interatomic potential of Doneghan and

Heald.^{44/} They considered the H_C , O, and T configurations, and found H_C to be the most stable with the lowest formation energy (0.86 eV). In addition, they have examined these three structures using the potential of Tome et al., finding O to be stable under the proper conditions, but that H_C was again the lowest energy configuration.^{45/} Unfortunately, these calculations do not seem compatible with the SE diffuse scattering data.

Very recent calculations by Imafuku, Yamamoto, and Doyama^{46/} shed more light on the situation. Using a Leonard-Jones potential fitted to the lattice parameter and vacancy formation energy, they studied various interstitial configurations in magnesium, including the four discussed in this work. They allowed 80 atomic relaxations and found two configurations with almost the same formation energy: the O configuration, with $E_F^I = 2.39$ eV; and a split dumbbell configuration situated along one of the close-packed rows in the basal plane, with $E_F^I = 2.36$ eV.

B. Recovery Model

In light of the well understood recovery behavior of the f.c.c. metals, the most significant features which a recovery model for magnesium must explain are the existence of two low temperature annealing peaks, both of which involve a combination of correlated and uncorrelated recovery, and the apparent dependence of the recovery processes in the second substage upon those in the first substage as evidenced by the radiation doping results. One possibility is the existence of two stable interstitial configurations, one responsible for the recovery in each substage. A number of the experimental observations could be explained with such a

model, including the presence of uncorrelated recovery in two separate substages. However, a two-interstitial model of this sort seems unnecessarily complicated compared to other metals without some experimental evidence to justify it.

A second simpler model is a single interstitial which has very different resonant modes for migration along the basal plane and perpendicular to the plane. The existence of the two radically different frequency factors provides support for a model of this nature. For this model, the substage I recovery is ascribed to the normal sequence of annealing events seen for the f.c.c.'s, but only for interstitial migration along the basal plane. With the restriction to two-dimensional motion, the number of close-pair configurations recombining in the first substage would be reduced, and would appear more like preliminary steps to long-range migration. This would give the observed broad substage with no uniquely resolved close-pair peaks. Interstitials in close-pair configurations perpendicular to the basal plane simply remain trapped in the first substage.

For further discussion, some assumptions must be made regarding the interstitial configuration and the interactions between interstitials and between interstitials and vacancies. Based upon the calculations of Imafuku et al. and SE's scattering results, the interstitial is assumed to be a split dumbbell located along a close-packed row in the basal plane. Interstitials and vacancies are assumed to attract; interstitials are assumed to repel when parallel to one another and attract when their axes (projected onto the basal plane) make angles of 60° or 120° with one

another. The last assumption takes into account the six-fold symmetry of the hexagonal basal plane.

These assumptions lead to three possibilities for the freely migrating substage I interstitial. A certain fraction will form clusters with other interstitials in the basal plane. There can only be two or, at most, three interstitials in each cluster so formed, since the assumed interaction is attractive only for interstitials in non-parallel orientations. Once three interstitials have clustered, any additional interstitial will be parallel to one of the three existing orientations and will thus be repelled. This result fits with SE's observations that clusters consisted of 2-3 interstitials, and that no dose-dependence was found for the cluster size. Some of the free interstitials will annihilate with vacancies, including some of the vacancies involved in off-plane close-pair configurations, thereby freeing the off-plane interstitial for migration in substage I. And finally, some of the free substage I interstitials will be trapped by vacancies or interstitials in parallel planes and held for recovery or clustering in substage II.

In substage II, interstitial motion perpendicular to the basal plane becomes possible. Correlated recovery will occur due to the recombination of the remaining off-plane close-pairs formed during irradiation and the annihilation of interstitials trapped by off-plane vacancies in substage I. Interstitials trapped by other off-plane interstitials may cluster or, for weak trapping at large separations, break free to undergo free migration. An additional contribution to free migration in substage II could be the reorientation of two trapped interstitials during migration perpendicular to the basal plane. The attractive interaction

could become repulsive if the jump process causes the two interstitials to be more nearly parallel; as a result, the two would detrap and migrate freely. The freely migrating substage II interstitial can either annihilate with a vacancy or cluster with other interstitials, leading to the growth in cluster size seen by SE for thermal annealing.

This model accounts for the major features observed for the radiation doping experiments, including the dependence of the second substage recovery on that of substage I. For doping of the first substage only, the doping treatment will leave behind vacancies, interstitial clusters, and interstitials trapped by off-plane vacancies and interstitials. The "new" free interstitials in substage I introduced by the second irradiation will have extra vacancies available for annihilation, including those in trapped configurations with off-plane interstitials normally reserved for recovery in substage II. Recombinations of the latter type will decrease the number of annealing events responsible for substage II recovery, as well as releasing the formerly trapped interstitials for free migration in substage I. The "new" interstitials can also form clusters with other interstitials in the same plane which are in trapping configurations with off-plane vacancies, thereby preventing these trapped interstitials from recombining in substage II as they normally would. The net result will be an enhancement in the recovery of the first substage due to the excess of vacancies accompanied by a reduction in the recovery which would be expected for the second substage due to the reduction of the trapped off-plane vacancy-interstitial pairs available for recombination; this is what was observed experimentally.

For doping of both substages, the doping treatment will result in interstitial clusters and an excess of vacancies. As for the previous case, the extra vacancies will contribute to an enhancement of the substage I recovery following the second irradiation because the freely migrating substage I interstitial will have more available annihilation sites. However, in contrast to the previous case, the "new" substage I free interstitial will not reduce the expected substage II recovery because there are no remaining trapped off-plane vacancy-interstitial pairs left for it to interact with. In fact, the excess vacancies should lead to an increase in the off-plane trapping of interstitials by vacancies compared to an undoped sample, resulting in an enhancement in the expected second substage recovery when these trapped pairs recombine. Thus the recovery should be enhanced in both substages, in agreement with the experimental findings.

There remain a number of questions unanswered for this model. Neither the form and strength of the interactions between interstitials nor the type of migratory jump processes held responsible for interstitial detrapping have been calculated or measured. Moreover, the configuration of the interstitial itself is not yet certain. It does seem clear, both from the existing experimental scattering data and from theoretical calculations, that the interstitial in magnesium is not like the split dumbbell along the c axis found in zinc. As a result, the recovery patterns of these two hexagonal metals might be expected to be quite different, as indeed they are. However, it is also clear that further calculations and, more importantly, good experimental data giving configurational information

about the single interstitial and its migration in magnesium (e.g., diffuse scattering or mechanical relaxation) are needed in order to develop an unambiguous model for the observed recovery behavior.

V. CONCLUSIONS

This study of magnesium after 1.0 MeV electron irradiations at 1.55 K provides new information regarding the nature of radiation damage and its recovery in this hexagonal metal.

The damage production rate is found to be $(3.57 \pm 0.03) \times 10^{-26}$ $\Omega\text{cm}/(e^- \text{cm}^2)$. There is no evidence for thermal annealing up to 4 K.

The low temperature recovery in magnesium is found to consist of two distinct broad substages between 4-14 K, both of which exhibit evidence for correlated and uncorrelated recovery. The two substages are found to have very different frequency factors for annealing, suggesting either two widely separated resonance modes for the recovery processes or two stable interstitial configurations. In addition, there is evidence that the recovery processes in the second substage are influenced by those in the first.

Theoretical calculations are found to favor either an octahedral configuration or a split dumbbell configuration along a close-packed row in the basal plane for the interstitial as opposed to the split dumbbell along the c axis found for zinc. A model for recovery is proposed using the split interstitial configuration in the basal plane which explains the first substage as being due to interstitial migration in the basal plane and the second to migration perpendicular to the plane.

APPENDIX A

ANALYSIS OF MAGNESIUM USED FOR SAMPLE GROWTH

A mass spectrographic analysis of the Dow triply distilled magnesium used to grow the magnesium samples revealed the following impurities in ppm, atomic:

Ta \leq 0.1

Sn 2

Ge \leq 3

Zn 0.3

Cu \leq 0.1

Ni \leq 0.2

Fe \leq 2

Cr \leq 0.8

V \leq 0.5

Ca 2

Cl 0.3

Si 2

Al 1

This is a semiquantitative analysis with an accuracy of \pm /x a factor of three.

APPENDIX B

DETAILS OF SAMPLE GROWTH AND THINNING PROCEDURES

For growing the magnesium samples, a cylindrical split graphite crucible was used with a cylindrical cavity machined along its axis to hold the magnesium charge. The sample mold was machined into one half of the crucible at the bottom of the cavity. The two crucible halves were held together by threaded clamps screwed onto either end of the crucible. In addition, the crucible was tapered outwards approximately 1° from top to bottom, and a clamp with matching taper was fitted snugly at the center of the crucible to keep the crucible halves tightly sealed during the melt.

Prior to each melt, a thin coating of aquadag diluted in alcohol was applied to the inner surfaces of the crucible, leaving a uniform thin film of graphite powder which prevented the grown sample from adhering to the crucible and being damaged during removal. The magnesium charge was etched in a dilute citric acid solution (5 g citric/95 cc water) to remove surface impurities. The charge was then placed in the crucible in an argon atmosphere and the crucible sealed at the top with a threaded cap to prevent extensive losses of the charge material to evaporation.

The crucible was suspended vertically in an oven and heated in a slowly flowing atmosphere of pure argon gas until all of the charge was melted. The crucible was located in the oven such that a temperature gradient of about 6°C/cm could be maintained over the sample region, with the bottom of the sample being coldest. The maximum temperature was held

for two hours to allow the hydrostatic pressure of the 19.5 cm column of molten charge to force magnesium down into the sample mold. Afterwards, the crucible was cooled to room temperature at a constant rate of about 35° C/hr.

The samples were washed in a solution of 20% nitric acid and 80% ethyl alcohol by volume to remove the surface layer of graphite. They were determined to be single crystals by visual inspection for grain boundaries and by examining Laue pictures of back-scattered x-rays, which gave the crystallographic orientation of each sample. Single crystals were used to avoid cold-working of the samples at low temperature due to differential thermal contractions of different grain orientations. The samples were etched to a uniform thickness of about 0.3 mm by one second dips in a solution of 15% nitric acid and 85% distilled water by volume, with rinses in distilled water between dips. The end tabs were coated with GE 7031 varnish and another series of dips performed to thin the sample legs to about 0.18 mm. The varnish was then removed by soaking the samples in acetone and a final cleaning and polishing etch done in the nitric/alcohol solution.

APPENDIX C
SIMPLE THEORY FOR RECOVERY KINETICS

For a single thermally-activated annealing process, the concentration of defects associated with the process is given as a function of time by

$$\frac{dc(t)}{dt} = -A f(c) e^{-E/kT} \quad (C-1)$$

where c is the concentration, t the time, A is a frequency factor, E the activation energy for the process, k is Boltzmann's constant, and T is the temperature. $f(c)$ is a function of the defect concentration which is dependent upon the order of the reaction.

For close-pair recovery, each pair annihilates independently of the rest. This gives $f(c) = c$, or first-order kinetics, and Equation (C-1) can be integrated to give

$$\frac{c(t)}{c_0} = \exp\left[-At e^{-E/kT}\right] \quad (C-2)$$

where c_0 is the initial defect concentration. The fractional recovery is independent of initial concentration.

For an annealing process involving long-range free migration of the interstitial in three dimensions, the recovery rate is proportional to the concentration of interstitials and the concentration of annihilation sites, or vacancies. Since these two concentrations are equal, $f(c) = c^2$, giving second-order kinetics, and Equation (C-1) integrates to

$$\frac{c(t)}{c_0} = \frac{1}{1 + c_0 A t e^{-E/kT}} \quad (C-3)$$

The fractional recovery occurs faster for increasing initial concentration.

Finally, for one-dimensional free interstitial migration, random walk theory predicts^{47/} $f(c) = c^3$, or third-order kinetics, for which Equation (C-1) integrates to give

$$\frac{c(t)}{c_0} = \frac{1}{\sqrt{1 + 2c_0^2 A t e^{-E/kT}}} \quad (C-4)$$

The fractional recovery occurs even faster than for second-order kinetics with increasing initial concentration.

As a result of the concentration dependence of the fractional recovery for second- and third-order processes, an annealing peak involving either of these processes will shift to lower temperatures with increasing initial concentrations. Nilan and Granato^{1/} have shown that the temperature of maximum recovery, T_m , for two different initial concentrations of defects will shift according to

$$\frac{\beta_1}{\beta_2} = \frac{\exp[E/kT_{m1} - E/kT_{m2}]}{(T_{m1}/T_{m2})^2}$$

where $(\beta_1/\beta_2) = (c_{01}/c_{01})$ for second-order kinetics and $(c_{01}/c_{01})^2$ for third-order kinetics.

Nilan and Granato have also calculated the approximate natural peak width at half maximum for a single first-order process, which they give as

$$\Delta T_{1/2} \approx \frac{2.4 k T_m^2}{E}$$

For higher order kinetics, the peak width broadens.

APPENDIX D

SLOPE CHANGE ACTIVATION ENERGY ANALYSIS

For a single thermally-activated process, Equation (C-1) can be re-written in terms of the resistivity ρ :

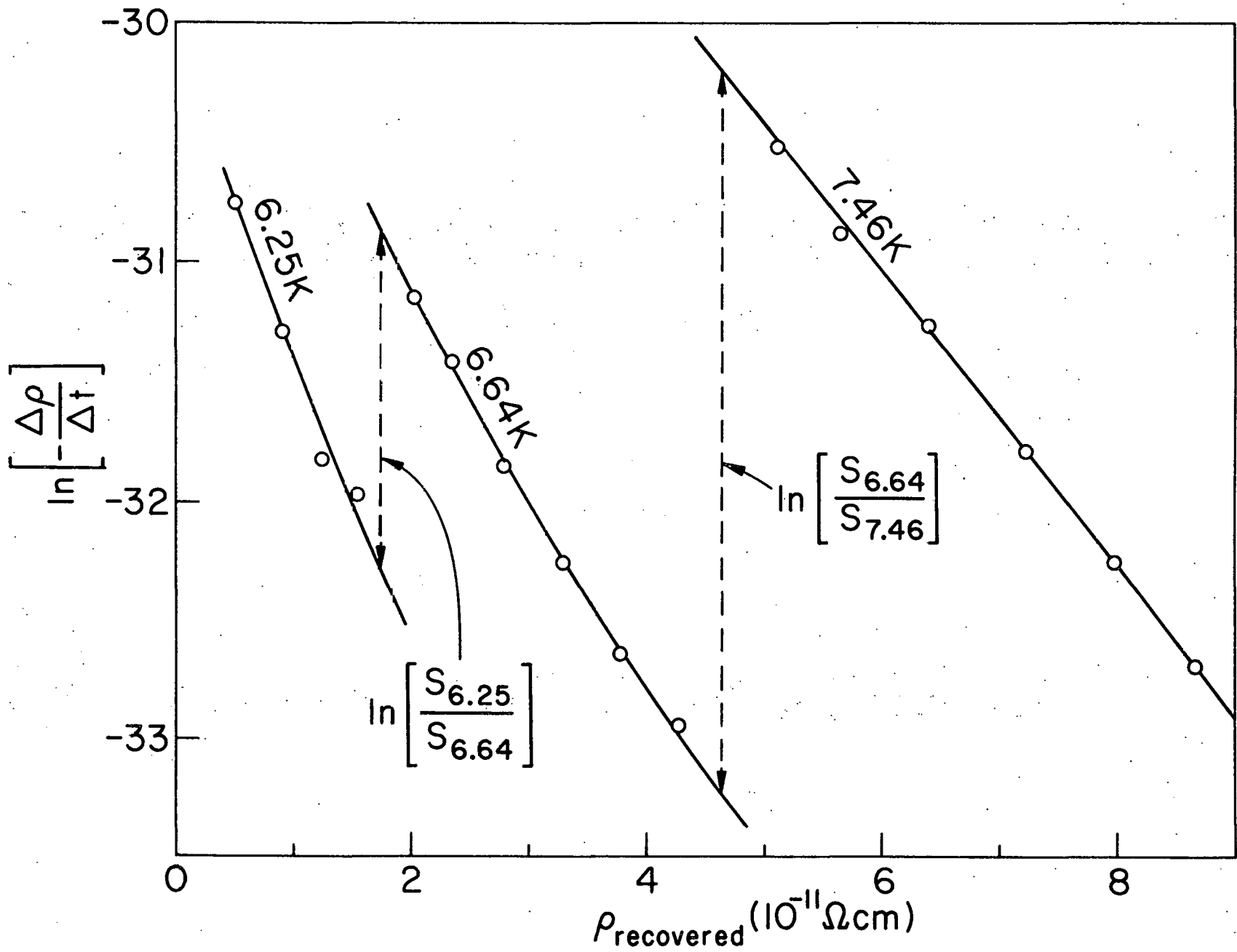
$$\frac{d\rho}{dt} = -Ag(\rho)e^{-E/kT} \quad (D-1)$$

During an isothermal annealing experiment, if the temperature is suddenly increased from T_1 to T_2 , the activation energy can be written as a function of the slopes of the two isothermals. From Equation (D-1) we have

$$\begin{aligned} E &= \frac{kT_1T_2}{T_2-T_1} \ln \left[\frac{\left(\frac{d\rho}{dt}\right)_{T=T_2}}{\left(\frac{d\rho}{dt}\right)_{T=T_1}} \right] \\ &= \frac{kT_1T_2}{T_2-T_1} \ln \left(\frac{S_2}{S_1} \right) \end{aligned} \quad (D-2)$$

The method of Dibbert et al.^{24/} involves determining the numerical derivative of each isothermal recovery curve at each measured isothermal annealing point. The natural logarithm of each derivative is then plotted as a function of the total recovery in resistivity at that annealing point, giving one curve of $\ln(d\rho/dt)$ vs. $\rho_{\text{recovered}}$ for each isothermal anneal. The value of $\ln(S_1/S_2)$ can then be determined from the amount of vertical discontinuity that occurs on the plot between isothermals 1 and 2 (see Figure 22, where the results for the first three anneals of isothermal run 2 have been plotted). The authors found this method gave a significant improvement in the uncertainty of the value of E over methods requiring an analytic fit to each isothermal.

Figure 22. Example of slope change method of activation energy determination for the first three isothermal anneals of isothermal run 2.



APPENDIX E

PRIMAK ACTIVATION ENERGY ANALYSIS

Consider the isothermal annealing of a first-order process distributed in activation energy. Defining the resistivity distribution function $P(E)$,

$$P(E) = c(E) f \quad (E-1)$$

where $c(E)$ is the fractional concentration of defects which anneal with activation energy E and f is the resistivity produced by 100% defects, Equation (C-2) can be written as

$$\begin{aligned} P(E) &= P_0(E) \exp(-Ate^{-E/kT}) \\ &= P_0(E) \Theta(t, T) \end{aligned} \quad (E-2)$$

$P_0(E)$ gives the original activation energy distribution before annealing, and $\Theta(t, T)$ is the characteristic annealing function which measures the amount of the original distribution swept out as the annealing time increases. The measured resistivity is given by

$$\rho = \int_0^{\infty} P(E) dE \quad (E-3)$$

After the first isothermal anneal for time t_1 at temperature T_1 , the distribution becomes

$$P_1(E) = P_0(E) \Theta(t_1, T_1) \quad (E-4)$$

Continuing for successive anneals, the distribution after the n^{th} anneal is given by

$$\begin{aligned} P_n(E) &= P_0(E) \theta(t_1, T_1) \theta(t_2, T_2) \dots \theta(t_n, T_n) \\ &= P_0(E) \left[\prod_{i=1}^{n-1} \theta(t_i, T_i) \right] \theta(t_n, T_n) \end{aligned} \quad (\text{E-5})$$

The measured defect resistivity remaining after the n^{th} anneal is

$$\rho_n = \int_0^{\infty} P_n(E) dE$$

or, from Equation (E-5),

$$\rho_n = \int_0^{\infty} P_0(E) \left[\prod_{i=1}^{n-1} \theta(t_i, T_i) \right] \theta(t_n, T_n) dE \quad (\text{E-6})$$

Taking the difference between two values of ρ measured at times t_1 and t_2 ($t_1 < t_2$) during the n^{th} anneal gives

$$\rho(t_1, T_n) - \rho(t_2, T_n) = \int_0^{\infty} P_0(E) \left[\prod_{i=1}^{n-1} \theta(t_i, T_i) \right] (\theta(t_1, T_n) - \theta(t_2, T_n)) dE \quad (\text{E-7})$$

Since the integrand is appreciably different from zero over a narrow range of E , $P_0(E)$ can be replaced to first order by a constant average value $P_{01}(\bar{E})$, for which Equation (E-7) becomes

$$\begin{aligned} \rho(t_1, T_n) - \rho(t_2, T_n) &= P_{01}(\bar{E}) \int_0^{\infty} \left[\prod_{i=1}^{n-1} \theta(t_i, T_i) \right] (\theta(t_1, T_n) - \theta(t_2, T_n)) dE \\ &= P_{01}(\bar{E}) \int_0^{\infty} I_{n1} dE \end{aligned} \quad (\text{E-8})$$

or,

$$P_{01}(\bar{E}) = \frac{\rho(t_1, T_n) - \rho(t_2, T_n)}{\int_0^{\infty} I_{n1} dE} \quad (\text{E-9})$$

where \bar{E} , the average value of the activation energy over the interval of integration, is given by

$$\bar{E} = \frac{\int_0^{\infty} E I_{n1} dE}{\int_0^{\infty} I_{n1} dE} \quad (\text{E-10})$$

For a second-order process the same theoretical approach is followed except that Equation (C-3) must be used:

$$P(E) = P_0(E) \left[1 + P_0 \frac{A}{F} t e^{-E/kT} \right]^{-1} \quad (\text{E-11})$$

After the n^{th} anneal,

$$P_n(E) = P_0(E) \left\{ 1 + P_0 \frac{A}{F} \left[\sum_{i=1}^{n-1} t_i e^{-E/kT_i} + t_n e^{-E/kT_n} \right] \right\}^{-1} \quad (\text{E-12})$$

and

$$\rho(t_n, T_n) = \int_0^{\infty} P_0(E) \left\{ 1 + P_0 \frac{A}{F} \left[\sum_{i=1}^{n-1} t_i e^{-E/kT_i} + t_n e^{-E/kT_n} \right] \right\}^{-1} dE \quad (\text{E-13})$$

Taking the difference between two values of ρ during the n^{th} anneal and replacing $P_0(E)$ by the constant average value $P_{02}(\bar{E})$ gives

$$\begin{aligned}
\rho(t_1, T_n) - \rho(t_2, T_n) &= P_{02}(\bar{E}) \int_0^{\infty} \left\{ \left[1 + P_{02} \frac{A}{F} \left(\sum_{i=1}^{n-1} t_i e^{-E/kT_i} + t_1 e^{-E/kT_n} \right) \right]^{-1} \right. \\
&\quad \left. - \left[1 + P_{02} \frac{A}{F} \left(\sum_{i=1}^{n-1} t_i e^{-E/kT_i} + t_2 e^{-E/kT_n} \right) \right]^{-1} \right\} dE \\
&= P_{02}(\bar{E}) \int_0^{\infty} I_{n2} dE \tag{E-14}
\end{aligned}$$

or

$$P_{02}(\bar{E}) = \frac{\rho(t_1, T_n) - \rho(t_2, T_n)}{\int_0^{\infty} I_{n2} dE} \tag{E-15}$$

where

$$\bar{E} = \frac{\int_0^{\infty} E I_{n2} dE}{\int_0^{\infty} I_{n2} dE} \tag{E-16}$$

REFERENCES

1. A. V. Granato and T. G. Nilan, Phys. Rev. 137, 1250 (1965).
2. J. W. Corbett, Phys. Rev. 137, A1806 (1965).
3. F. W. Young, Jr., J. Nucl. Mater. 69-70, 310 (1978).
4. P. S. Gwozdz and J. S. Koehler, Phys. Rev. B 8, 3616 (1973).
5. H. Cope, G. Sulpice, C. Minier, H. Bilger, and P. Moser, International Conference on Vacancies and Interstitials in Metals, Julich, 1968 (unpublished).
6. H. Vandenborre, J. Nihoul, and L. Stals, Cryst. Lattice Defects 5, 89 (1974).
7. H. Neely, Radiat. Eff. 3, 189 (1970).
8. R. R. Coltman, C. E. Klabunde, J. K. Redman, and A. L. Southern, Radiat. Eff. 7, 235 (1971).
9. P. Ehrhart and B. Schönfeld, Phys. Rev. B 19, 3896 (1979).
10. T. N. O'Neal and R. L. Chaplin, Phys. Rev. B 5, 3810 (1972).
11. B. Schönfeld and P. Ehrhart, paper presented at the General Meeting of the American Physical Society, Phoenix, Arizona, March 1981.
12. P. Tzanetakis, J. Hillairet, and G. Revel, Phys. Status Solidi B 75, 433 (1976).
13. P. G. Shewmon, Trans. AIME 206, 918 (1956).
14. V. Levy, J. Hillairet, D. Schumacher, G. Revel, and T. Chaudron, International Conference on Vacancies and Interstitials in Metals, Julich, 1968 (unpublished).
15. J. W. Corbett, Solid State Physics, edited by F. Seitz and D. Turnbull (Academic, New York, 1966), Supplement 7, Chapter 6.
16. M. J. Berger and S. M. Smeltzer, Tables of Energy Losses and Ranges of Electrons and Positrons (NASA Scientific and Technical Information Division, Washington, D.C., 1964).

17. A. C. Anderson, Temperature, Its Measurement and Control in Science and Industry, edited by R. A. Scribner and E. D. Adams (Instrument Society of America, Pittsburgh, 1972), Vol. 4, Part 2, p. 773.
18. Y. S. Touloukian, ed., Thermophysical Properties of Matter (IFI/Plenum, New York-Washington, 1970), Vol. 1, p. 207.
19. J. P. Harrison, *J. Low Temp. Phys.* 17, 43 (1974).
20. G. L. Pollack, *Rev. Mod. Phys.* 41, 48 (1969).
21. N. S. Snyder, *Cryogenics* 10, 89 (1970).
22. W. H. Keesom, B. F. Saris, and L. Meyer, *Physica* 7, 817 (1940).
23. K. Fischer, *Phys. Kond. Mater.* 6, 171 (1967).
24. H. J. Dibbert, K. Sonnenberg, W. Schilling, and U. Dedek, *Radiat. Eff.* 15, 115 (1972).
25. W. Primak, *Phys. Rev.* 100, 1677 (1955).
26. See for example W. Bauer, J. W. Deford, J. S. Koehler, and J. W. Kauffman, *Phys. Rev.* 128, 1497 (1962).
27. See for example F. Dworschak, K. Herschback, and J. S. Koehler, *Phys. Rev.* 133, A293 (1964).
28. J. W. Corbett, Chapter 9 in ref. (15).
29. T. N. O'Neal and R. L. Chaplin, *Phys. Letters* 26A, 453 (1968).
30. W. Schilling, G. Burger, K. Isebeck, and H. Wenzl, Vacancies and Interstitials in Metals, edited by A. Seeger, D. Schumacher, W. Schilling, and J. Diehl (Elsevier, New York, 1970), p. 255.
31. R. L. Chaplin and H. M. Simpson, *Phys. Rev.* 163, 587 (1967).
32. P. Ehrhart, p. 200 in ref. (3).
33. P. Ehrhart and U. Schlagheck, Fundamental Aspects of Radiation Damage in Metals, edited by M. T. Robinson and F. W. Young, Jr. (ERDA Report CONF-751006 P2, Springfield, Virginia, 1976), p. 839.
34. B. Schönfeld and P. Ehrhart, *Phys. Rev. B* 8, 3905 (1979).
35. R. A. Johnson, p. 295 in ref. (3).
36. P. H. Dederichs, Fundamental Aspects of Radiation Damage in Metals, edited by M. T. Robinson and F. W. Young, Jr. (ERDA Report CONF-751006 P1, Springfield, Virginia, 1976), p. 187.

37. P. H. Dederichs, C. Lehmann, H. R. Schober, A. Scholz, and R. Zeller, p. 176 in ref. (36).
38. This is the low temperature value of a calculated from the room temperature lattice parameter ($a = 3.2094 \text{ \AA}$) and density of magnesium given in W. B. Pearson, Handbook of Lattice Spacings and Structure of Materials (Pergamon, New York, 1967), Vol. 2, and the low temperature density of magnesium given in ref. (39).
39. L. J. Slutsky and C. W. Garland, Phys. Rev. 107, 972 (1957).
40. J. Frenkel and T. Kontorova, Phys. Z. Sowjetunion 13, 1 (1938).
41. J. S. Koehler, Phys. Rev. B 18, 5333 (1978).
42. C. N. Tome, A. M. Monti, and E. J. Savino, Phys. Status Solidi B 92, 323 (1979).
43. H. K. Sahu, S. Srinivasan, and K. Krishan, Radiat. Eff. Letters, 50, 73 (1980).
44. M. Doneghan and P. T. Heald, Phys. Status Solidi A 30, 403 (1975).
45. H. K. Sahu, S. Srinivasan, and K. Krishan, Pramana 15, 189 (1980).
46. M. Imafuku, R. Yamamoto, and M. Doyama, presented at the Yamada Conference V on Point Defects and Defect Interactions in Metals (Kyoto, Japan, 1981), to be published.
47. W. M. Lomer and A. H. Cottrell, Philos. Mag. 46, 711 (1955).